bioRxiv preprint doi: https://doi.org/10.1101/835603; this version posted November 10, 2019. The copyright holder for this preprint (which was not certified by peer review) is the author/funder, who has granted bioRxiv a license to display the preprint in perpetuity. It is made available under aCC-BY-ND 4.0 International license.

A TBX5 dosage-sensitive gene regulatory network for human congenital heart disease

Irfan S. Kathiriya[1,2,3]*, Kavitha S. Rao[1,2,3], Giovanni Iacono[4], W. Patrick Devine[1,5], Swetansu K. Hota[1,2], Michael H. Lai[1,2], Bayardo I. Garay[1,2,3], Reuben Thomas[1], Andrew P. Blair[1,8], Henry Z. Gong[8], Lauren K. Wasson[6,7], Piyush Goyal[1,2], Tatyana Sukonnik[1,2], Gunes A. Akgun[1,2], Laure D. Bernard[1,2], Brynn N. Akerberg[9], Fei Gu[9], Kai Li[9], William T. Pu[9,10], Joshua M. Stuart[8], Christine E. Seidman[6,7], J. G. Seidman[6], Holger Heyn[4,11], Benoit G. Bruneau[1,2,12,13]*

1. Gladstone Institutes, San Francisco, CA, USA.

2. Roddenberry Center for Stem Cell Biology and Medicine at Gladstone, San Francisco, CA, USA

3. Department of Anesthesia and Perioperative Care, University of California, San Francisco, CA, USA

4. CNAG-CRG, Centre for Genomic Regulation (CRG), Barcelona Institute of Science and Technology (BIST), Barcelona, Spain;

5. Department of Pathology, University of California, San Francisco, CA, USA

6. Department of Genetics, Harvard Medical School, Boston, MA USA

7. Howard Hughes Medical Institute, Division of Cardiovascular Medicine, Brigham and Women's Hospital, Boston, MA USA

8. Department of Biomolecular Engineering, University of California, Santa Cruz, Santa Cruz, CA, USA

9. Department of Cardiology, Boston Children's Hospital, Boston, MA, USA

10. Harvard Stem Cell Institute, Harvard University, Cambridge, MA, USA

11. Universitat Pompeu Fabra, Barcelona, Spain

bioRxiv preprint doi: https://doi.org/10.1101/835603; this version posted November 10, 2019. The copyright holder for this preprint (which was not certified by peer review) is the author/funder, who has granted bioRxiv a license to display the preprint in perpetuity. It is made available under aCC-BY-ND 4.0 International license.

12. Department of Pediatrics, University of California, San Francisco, CA, USA

13. Cardiovascular Research Institute, University of California, San Francisco, CA, USA

* Authors for correspondence: irfan.kathiriya@ucsf.edu, benoit.bruneau@gladstone.ucsf.edu

Abstract

Haploinsufficiency of transcriptional regulators causes human congenital heart disease (CHD) [1]. This observation predicts gene regulatory network (GRN) imbalances [2], but the nature of dosage-vulnerable GRNs and their contribution to human cardiogenesis and CHDs are unknown. Here, we define transcriptional consequences of reduced dosage of the CHD transcription factor TBX5 during human cardiac differentiation from induced pluripotent stem (iPS) cells. Single cell RNAseq revealed that transcriptional responses to reduced TBX5 levels are not homogeneous, and instead, discrete sub-populations of cardiomyocytes exhibit dysregulation of distinct TBX5 dose-sensitive genes related to cellular phenotypes and CHD-associated genetics. Cellular trajectory inference revealed TBX5 dosage-dependent differentiation paths, with implications for cardiac developmental identity. GRN analysis of the single cell RNAseq data identified vulnerable nodes enriched for CHD genes, implicating a critical sensitivity to TBX5 dosage in cardiac network stability. A novel GRN-predicted genetic interaction between *TBX5* and *MEF2C* was validated in mouse, revealing a highly dosage-sensitive pathway for CHD. Our results reveal unforeseen complexity and exquisite sensitivity to TBX5 dosage in discrete sub-populations of iPSC-derived cardiomyocytes, providing mechanistic insights into human CHDs and quantitative transcriptional regulation in disease.

Introduction

CHDs are a leading cause of childhood morbidity and mortality, and incidence of CHD is estimated to be ten-fold higher in human fetuses than live births [3,4]. Many human mutations

bioRxiv preprint doi: https://doi.org/10.1101/835603; this version posted November 10, 2019. The copyright holder for this preprint (which was not certified by peer review) is the author/funder, who has granted bioRxiv a license to display the preprint in perpetuity. It is made available under aCC-BY-ND 4.0 International license.

linked to CHD predict reduction in dosage of transcriptional regulators, including transcription factors (TFs) and chromatin-modifying genes [1]. Despite advances in tracing the roles of individual factors, how altered dosage of transcriptional regulators translates to altered transcriptional activity is not known, nor is it known how these altered GRNs disrupt heart development, resulting in CHD.

Heterozygous mutations in the T-box TF gene *TBX5* cause Holt-Oram syndrome (HOS) [5,6], which presents with upper limb defects, CHDs, diastolic dysfunction, or arrhythmias. In humans, homozygous *TBX5* loss of function is presumed to cause fetal demise. Altered expression of select genes in mice *in vivo* demonstrate a stepwise sensitivity to reductions in *Tbx5* dosage [7,8]. These findings suggest that a reduction in TBX5 dosage perturbs downstream gene expression, but the overall disrupted networks and mechanisms are not understood.

Mechanistic investigation of human CHD has been hampered by a lack of relevant and tractable models. Human heart tissue is largely inaccessible for molecular analysis, and pathological or surgical specimens are limited. However, induced pluripotent stem (iPS) cells, genome editing, directed differentiation, and single cell RNAseq together provide a human cellular platform for gene-centered cardiac disease modeling at single cell resolution. In considering how transcriptional regulator haploinsufficiency might cause CHD, at least two scenarios are possible: 1. That reduced dosage affects genes only in specific anatomical locations, such as the atrial septum. 2. That reduced dosage affects cardiac gene expression broadly, but altered programs manifest as morphologic defects only in structures most sensitive to the disturbance. The first scenario would make it challenging to discover altered gene expression in 2-dimensional cultures if susceptible cell types are absent. The second may predict that homogeneous changes in gene expression might be detected in that context, as corroborated by bulk RNAseq studies of heterozygous human iPS cell models of CHD [9-11]. However, it is likely that relevant, discrete alterations in a complex cell mixture were not

bioRxiv preprint doi: https://doi.org/10.1101/835603; this version posted November 10, 2019. The copyright holder for this preprint (which was not certified by peer review) is the author/funder, who has granted bioRxiv a license to display the preprint in perpetuity. It is made available under aCC-BY-ND 4.0 International license.

detected in those studies. Therefore, how reduced dosage of a transcriptional regulator alters GRNs in susceptible cells leading to CHD remains unclear.

Impaired human cardiac differentiation and function by reduced TBX5 dosage

To determine a role for TBX5 dosage in human cardiac biology, we created an allelic series of human iPS cells mutant for *TBX5* by using CRISPR/Cas9-mediated genome editing, to target exon 3 of *TBX5* at the start of the essential T-box domain (Fig. 1a). We isolated targeted iPS cell lines: control (*TBX5*$^{+/+}$), heterozygous (*TBX5*$^{in/+}$) and homozygous (*TBX5*$^{in/del}$ and *TBX5*$^{PuR/PuR}$) mutants (Fig. 1b, Extended Data 1). TBX5 protein levels in cardiomyocytes differentiated from these lines were diminished in *TBX5*$^{in/+}$ and absent in *TBX5*$^{in/del}$ and *TBX5*$^{PuR/PuR}$ cells (Fig. 1c), consistent with a dosage-step allelic series of mutant *TBX5* loss-of-function cell lines.

We observed reduced cardiomyocyte differentiation efficiency, a delay in onset of beating, and worsening sarcomere disarray, by graded loss of *TBX5* (Fig. 1d-j, Extended Data 2). Patch clamp analysis revealed lengthened action potentials (AP) in *TBX5*$^{in/del}$ cells (Fig. 1k, l; APD90, adj p-value<0.04 by Holm-Sidak test[12]), consistent with previous findings [13-15]. Fluo-4 imaging measurements uncovered protracted calcium transient duration in *TBX5*$^{in/del}$ and *TBX5*$^{PuR/PuR}$ cells (T90 down, adj p-value<9E-4 by Holm-Sidak test), with an intermediate defect in *TBX5*$^{in/+}$ cells (adj p-value<0.01) (Fig. 1m, n), consistent with findings in murine postnatal atrial CMs [16]. These findings may underlie diastolic dysfunction in HOS in mice and humans [17].

Resolving TBX5 dosage-sensitive transcriptomes during human cardiac differentiation

To determine if reduced TBX5 dosage alters gene expression in potentially vulnerable cell types, we used a droplet-based single cell RNAseq method with cells collected from

bioRxiv preprint doi: https://doi.org/10.1101/835603; this version posted November 10, 2019. The copyright holder for this preprint (which was not certified by peer review) is the author/funder, who has granted bioRxiv a license to display the preprint in perpetuity. It is made available under aCC-BY-ND 4.0 International license.

parental WTC11, control *TBX5*$^{+/+}$, and mutant *TBX5* (*TBX5*$^{in/+}$, *TBX5*$^{in/del}$) genotypes during directed cardiac differentiation (Fig. 2a). Heterogeneous cell populations composed of cardiac precursors (CP) at day (d) 6, and cardiomyocytes (CMs) at d11 or d23, were harvested. We interrogated 64,396 cells with an average normalized read depth of 88,234 reads per cell (Fig. 2b-d; Extended Data 3). At d6, we identified 11 cell clusters, representing at least four cell types, including *POU5F1*$^{+}$ pluripotent cells, *MESP1*$^{+}$ mesoderm, *ISL1*$^{+}$ cardiac precursors and nascent *TNNT2*$^{+}$ cardiomyocytes (Extended Data 3). At d11 and d23, differentiated cell types were identified by specific marker genes (Extended Data 3). This included a diversity of *TBX5*$^{+}$ cell types, comprising very few *PLVAP*$^{+}$ endothelial cells or *TTR*$^{+}$ endodermal cells, some *COL1A1*$^{+}$ fibroblasts and, most abundantly, *TNNT2*$^{+}$ cardiomyocytes (Extended Data 3, 4). All of these major cell types were present and detected in each *TBX5* genotype at d11 or d23 (Extended Data 3).

We applied this classification of human cell types to learn more about the genes that contribute to CHDs. We examined the expression of 376 CHD-associated candidate genes, compiled from [18-25], across the major cell types regardless of *TBX5* genotypes at d23 (Extended Data 4, Supplemental Table 1). For many CHD-associated genes, we observed enrichment of gene expression in CMs (e.g.*TBX5, FOXH1*, *ARID1A*, *EP300*, *KDM6A*, *PKD1*; adj p-value<0.05 by Wilcoxon Rank Sum test), fibroblasts (e.g. *SMARCA2, PITX2, ZEB2, HAND2*; adj p-value<0.05), endoderm (e.g. *TBX3, WDR5, SALL4, NODAL*; adj p-value<0.05), endothelial cells (e.g. *FGFR1, TGFBR2, SHANK3, KCNJ2*; adj p-value<0.05) or other cell types (Extended Data 4). This gene expression dataset provides a resource that helps identify progenitors to these cell types and may allow further categorization of human CHD-associated candidate genes.

TBX5 dose-dependent cellular trajectories during human cardiac differentiation

bioRxiv preprint doi: https://doi.org/10.1101/835603; this version posted November 10, 2019. The copyright holder for this preprint (which was not certified by peer review) is the author/funder, who has granted bioRxiv a license to display the preprint in perpetuity. It is made available under aCC-BY-ND 4.0 International license.

To assess if altered transcriptional states in *TBX5* mutant cells reflected changes in paths of differentiation, we inferred cellular trajectories of each *TBX5* genotype in our allelic series using the R package URD [26], which predicts cellular chronology based on user-determined origins and ends. We defined *POU5F1*$^{+}$ cells from d6 as a root and each d23 cluster as an individual tip in a pseudotime tree (Fig. 2b-d, Extended Data 5). *TBX5*$^{in/+}$ cells followed a path similar to wildtype and control (collectively "WT) cells during differentiation to CMs (Fig. 2e, f, dashed lines), but within the shared branch, a tip occupied by *TBX5*$^{in/+}$ CMs (red arrowhead) was disparate from wildtype (black arrowhead) and control, demonstrating *TBX5*$^{in/+}$ CMs distinct from WT. In contrast, *TBX5*$^{in/del}$ cells deviated from the differentiation path (Fig. 2g, blue dashed line, blue arrowheads). We identified several genes (e.g. *NAV1, TECRL, LAMA4,* and *NPPA*), which were positively correlated with pseudotime (rho≥|0.4|, p-value<0.05 by two-sided *t* test) in the WT/*TBX5*$^{in/+}$ branch, but not in the *TBX5*$^{in/del}$ branch (Z-score≥15 by difference in rho), suggesting that these genes were not activated properly in *TBX5*$^{in/del}$ cells (Fig. 2h, i, Extended Data 5). Likewise, we identified several genes (e.g. *DES, TBX2, RSPO3,* and *LBH*) that positively correlated with pseudotime in *TBX5*$^{in/del}$ cells (rho≥|0.4|, p-value<0.05), but not in wildtype cells (Z-score≥15) (Fig. 2j, Extended Data 5), signifying that these genes are inappropriately deployed in *TBX5*$^{in/del}$ cells.

To identify genes that may determine one cell trajectory route from another, we assessed differential gene expression between imputed intermediates, which we considered as potential precursors, within branches proximal to *TBX5* genotype-specific tips. We compared these intermediate branches of cells that distinguish the cell trajectory route to CMs of wildtype, control and *TBX5*$^{in/+}$ from *TBX5*$^{in/del}$ (Fig. 2k, segments 69 vs. 70). We identified several differentially expressed genes, including structural genes (e.g. *MYL3*, *TTN*, *MYH6*, *TNNT2*, *TNNI1*; adj p-value<0.05 by Wilcoxon Rank Sum test), calcium handling genes (*PLN*, *ATP2A2, RYR2*; adj p-value<0.05), secreted factors (*WNT2*, *FGFR1*; adj p-value<0.05), and cardiac TFs (*IRX4*, *HAND2*; adj p-value<0.05) (Extended Data 5). Of note, expression of the CHD-

bioRxiv preprint doi: https://doi.org/10.1101/835603; this version posted November 10, 2019. The copyright holder for this preprint (which was not certified by peer review) is the author/funder, who has granted bioRxiv a license to display the preprint in perpetuity. It is made available under aCC-BY-ND 4.0 International license.

associated cardiac transcription factor *NKX2-5*, a transcriptional partner of TBX5 [7,27,28], was differentially expressed between intermediate branches of the URD tree that distinguish wildtype/control/*TBX5*$^{in/+}$ *TNNT2*$^{+}$ cells from *TBX5*$^{in/del}$ *TNNT2*$^{+}$ cells (Fig. 2l; adj p-value<1E-300 by Wilcoxon Rank Sum test). Onset of *NKX2-5* expression was delayed in *TBX5*$^{in/del}$ cells (adj p-value<0.05 by Bonferroni-Holm multiple testing correction), along with a module of genes (e.g. *PARP1, RPL37, KIAA1462* and *ATP1A1*; adj p-value<0.05), concomitant with *NKX2-5* expression (Fig. 2l, Extended Data 5), providing a potential molecular explanation for a delay of onset of beating by *TBX5* loss (Fig. 1e).

Quantitative transcriptomic responsiveness to reduced TBX5 dosage in cardiomyocytes

TBX5 genotype-specific clusters emerged among cardiomyocytes at d11 (Fig. 2c), and *TBX5* genotype-specific segregation was more striking at d23, particularly in *TNNT2*$^{+}$ cells (Fig. 2d). We focused on *TNNT2*$^{+}$ clusters at d23 (Fig. 3a, b) and d11 (Extended Data 6). We constructed a phylogenetic tree relating 25 different *TNNT2*$^{+}$ cell clusters (Fig. 3c), and observed heterogeneity of gene set enrichment among WT or *TBX5*$^{in/+}$ clusters (Fig. 3d), implying putative CM subtypes. Some CM subtypes did not fit conventional categorization based on anatomy. We searched for differentially expressed genes, by pair-wise comparisons of related subtypes between *TBX5* genotypes. To identify *TBX5* genotype-specific differences within a CM subtype, we compared clusters enriched for WT to related clusters enriched for *TBX5*$^{in/+}$ or *TBX5*$^{in/del}$ cells (Fig. 3d-k). We discovered only a few common changes in gene expression amongst pair-wise cluster comparisons of WT vs *TBX5*$^{in/+}$ clusters, such as *NPW* and *PLN* (Fig. 3d-i; adj p-value<0.05 by Wilcoxon Rank Sum test). We also discerned differences in gene expression based on cluster-specific comparisons (adj p-value<0.05 by Wilcoxon Rank Sum test), implying discrete cell subtype-sensitivity to TBX5 haploinsufficiency (Fig. 3d-i) or *TBX5* loss (Extended Data 7). We also compared related *TBX5* genotype-specific

bioRxiv preprint doi: https://doi.org/10.1101/835603; this version posted November 10, 2019. The copyright holder for this preprint (which was not certified by peer review) is the author/funder, who has granted bioRxiv a license to display the preprint in perpetuity. It is made available under aCC-BY-ND 4.0 International license.

cell clusters at a lower resolution of Louvain clustering and discovered genes that were differentially expressed across reduced TBX5 dosage in a variety of patterns (Fig. 3j, k). Quantitative changes in gene expression level were apparent across *TBX5* genotypes (for example, *PLN, FYXD1*; adj p-value<0.05 by Wilcoxon Rank Sum test), as were changes in both expression level and percentage of expressing cells (e.g. *RSPO3, NPPA, TECRL, DES*) (Fig. 3k).

This differentially expressed gene set was enriched for electrophysiology (EP)-related genes (FDR<0.05, Fig. 3l), which are implicated in membrane depolarization (*SCN5A*), calcium handling (*RYR2*, *ATP2A2*, and *PLN*) and arrhythmias (*TECRL*) (Fig. 3e, g, i, k, l). Several altered transcripts were encoded by other genes implicated in CHD (*CITED2, MYOCD, ANKRD1*) (Fig. 3e, g, i, k, l). Some TBX5-dependent genes that were previously associated with CHD or arrhythmias by genome-wide association studies (GWAS) were identified (Fig. 3l). We uncovered *IGFBP7, FRAS1, MYH7B* and *SMCHD1* for CHD (odds ratio 3.2, FDR<0.03) and 47 reported genes for arrhythmias (for example, *PLN, HCN4, SCN5A, GJA1*, *PITX2* and *TECRL*; odds ratio 9.0, FDR<1.9E-39) among TBX5-sensitive genes at day 23 (Fig. 3m, Supplementary Table 2).

Using orthogonal assays at single cell resolution, we found that *TBX5* dosage-dependent downregulation of *NPPA* was evident in CMs by RNAscope ($TBX5^{in/+}$, p<0.05; $TBX5^{in/del}$ or $TBX5^{PuR/PuR}$, p<1E-4 by Student's t-test), consistent with a TBX5-dependent rheostatic regulation of this gene in mouse [7,8]. Loss of DES in $TBX5^{in/+}$ and recovery in $TBX5^{in/del}$ was detected in CMs by flow cytometry (Extended Data 8, p-value<1E-4 by Chi-Square test), corroborating some human *TBX5* dose-dependent sequelae.

Comparisons of biological replicates at d23 showed significant overlap of TBX5-dependent genes for WT vs. $TBX5^{in/+}$ (p-value<2.466e-9 by hypergeometric test) or WT vs. $TBX5^{in/del}$ (p-value<5.410e-6) (Extended Data 9, 10). The differences in gene expression between biological replicates likely reflect a combination of technical variability and biological

bioRxiv preprint doi: https://doi.org/10.1101/835603; this version posted November 10, 2019. The copyright holder for this preprint (which was not certified by peer review) is the author/funder, who has granted bioRxiv a license to display the preprint in perpetuity. It is made available under aCC-BY-ND 4.0 International license.

stochasticity that, as in patients with *TBX5* mutations, may explain variable expressivity of disease for a given mutation. Since modifiers in different genetic backgrounds might modulate phenotypic effects, we assessed iPSC lines of *TBX5* mutants in an independent genetic background (PGP1, from a Caucasian male, compared to WTC11 from a Japanese male, Extended Data 11). Comparisons of TBX5-dependent genes in d23 *TNNT2*$^{+}$ cells showed significant overlap between WTC11 vs. *TBX5*$^{in/+}$ and PGP1 vs. *TBX5*$^{in/+}$ (p-value<1.174e-8 by hypergeometric test) or WTC11 vs *TBX5*$^{in/del}$ and PGP1 vs. *TBX5*$^{del/del}$ (p-value<7.260e-15) (Extended Data 11, 12), proportionally similar to biological replicates (Extended Data 9, 10). These results demonstrate reproducible TBX5 dosage-dependent alterations from independent experiments, genetic backgrounds, and gene targeting strategies.

To assess if changes to TBX5 dose-sensitive genes were largely direct or indirect TBX5 targets, we examined TBX5 occupancy in human iPSC-derived CMs from a published dataset [10]. We found correlations of TBX5 occupancy near TBX5 dosage-vulnerable gene sets (Fig. 3l, m, and Extended Data 13, 14; for example, odds ratio 6.9 for all TBX5-dependent human genes; FDR<1.9E-178), suggesting our identified genes may be direct TBX5 targets. TBX5 cooperates with GATA4 for cardiac gene regulation [10,28,29]; we also observed that GATA4 occupancy [10] with TBX5 was highly associated near TBX5-dependent genes (Fig. 3l, m, and Extended Data 13, 14; for example, odds ratio 6.4 for all TBX5-dependent human genes; FDR<1.3E-155), indicating that GATA4 may have a role modulating TBX5 dosage-sensitive genes.

Susceptible human gene regulatory networks for congenital heart disease

Since CHD-associated and arrhythmia-related genes were enriched among TBX5-dependent genes, we deduced that TBX5 may be vital for preserving the integrity of cardiac gene regulatory networks (GRNs). To evaluate the role of TBX5 dosage for regulating GRNs,

bioRxiv preprint doi: https://doi.org/10.1101/835603; this version posted November 10, 2019. The copyright holder for this preprint (which was not certified by peer review) is the author/funder, who has granted bioRxiv a license to display the preprint in perpetuity. It is made available under aCC-BY-ND 4.0 International license.

we used bigSCale2 [30] to independently infer putative GRNs from single cell expression data of *TNNT2*$^{+}$ cells at d6, d11 and d23 of each *TBX5* genotype (Fig. 4a, b, Extended Data 15). This allows for quantitative prediction of the biological importance of genes in a regulatory network reconstructed with bigSCale2, by applying the concept of "pagerank" [30], first devised to rank the importance of websites via numerical weighting [31], to discover genes with a loss in importance (i.e. centrality) among *TBX5* genotypes. By comparing nodes from inferred networks of WT to *TBX5*$^{in/+}$ or *TBX5*$^{in/del}$, we uncovered several nodes that displayed reduced pagerank centrality at specific time points and levels of reduced TBX5 dosage (Fig. 4a-c, Extended Data 15). These included *RYR2* and twenty CHD-associated genes (for example, *GATA6*, *HAND2*, *SMAD2,* $p<2.2e-5$ by hypergeometric test,) (Fig. 4c, d, Extended Data 15), consistent with independent analysis from differential gene expression. For example, at d11, pagerank centrality of the CHD-associated TF *SMAD2* was absent in *TBX5*$^{in/+}$ cells (Fig. 4a-c, top 5% of all changes), indicating an impairment of *SMAD2* function. Centrality of the cardiac development-related TF *MEF2C*, which is necessary for heart development [32], was substantially reduced by heterozygosity or loss of *TBX5* at d11 (Fig. 4a-c, top 5% cutoff). *MEF2C* gene expression was unchanged by reduced TBX5 dosage, suggesting a change in *MEF2C* functional connectivity. These altered GRNs show that TBX5 dosage is critical for maintaining cardiac network stability, and unveil potential genetic interactions disrupted in TBX5-dependent CHDs.

To further investigate the predicted relationship between *TBX5* and *MEF2C* within a dosage-sensitive CHD-associated GRN, we used a complementary approach using bigSCale2, to identify gene-gene correlations with *TBX5* expression in individual *TNNT2*$^{+}$ cells across timepoints and *TBX5* genotypes (Fig. 4e). Genes highly co-expressed with *TBX5* (Pearson coefficient >0.5) regardless of *TBX5* genotype suggested potential cell autonomous effects by *TBX5* dosage (for example, *PLN*, *RYR2*, *TTN*), while those with high anti-correlation (Pearson coefficient <-0.5) suggested non-cell autonomous effects (for example, *HES1, TLE1, CBX1,*

bioRxiv preprint doi: https://doi.org/10.1101/835603; this version posted November 10, 2019. The copyright holder for this preprint (which was not certified by peer review) is the author/funder, who has granted bioRxiv a license to display the preprint in perpetuity. It is made available under aCC-BY-ND 4.0 International license.

ETV4, ID4, FGFR1). *MEF2C* expression was among the highest correlated with *TBX5* expression and demonstrated greatest *TBX5*-dependent decrease of pagerank (Fig. 4c, e) or degree (i.e. putative number of target genes, Supplemental Table 3) at d11, further suggesting *MEF2C* as a candidate for mediating TBX5 dose-sensitive regulatory effects. Multiple genes that correlated with *MEF2C* displayed diminished levels of degree by reduced TBX5 dosage (for example, *SMYD1, PDK1, MYOCD, TTN, RYR2*; top 5% cutoff) (Fig. 4f, Supplementary Table 3), supporting a potential explanation for changes to *MEF2C* functional connectivity in a TBX5 dosage-sensitive GRN.

We evaluated the predicted genetic interaction between *TBX5* and *MEF2C in vivo*. We used a hypomorphic allele of *Tbx5* (*Tbx5*^{CreERT2IRES2xFLAG}, abbreviated *Tbx5*^{CreERT2}) [33], which we further characterized (Extended Data 16) to probe for a potentially highly-sensitive genetic interaction between *Tbx5* and a null allele of *Mef2c (Mef2c*^{del}*)* [32]. *Tbx5*$^{CreERT2/+}$*;Mef2c* $^{del/+}$ mice were underrepresented at weaning (Fig. 5a). By histology, we detected muscular (n=3 of 4) or membranous (n=1 of 4) VSDs in compound heterozygous embryos at E14.5, which were not apparent in *Tbx5*$^{CreERT2/+}$ or *Mef2c* $^{del/+}$ embryos (Fig. 5b-k). These findings demonstrate a highly-sensitive genetic interaction between *Tbx5* and *Mef2c* in mouse *in vivo*, consistent with prediction from the human TBX5 dose-sensitive GRN.

We speculated that MEF2C may play a direct role to co-regulate TBX5-dependent gene expression. Chromatin occupancy [34] of TBX5, MEF2c, and MEF2a (also predicted to be part of the TBX5-dependent GRN) was highly correlated near TBX5-sensitive human or mouse genes (for example, *HAND2*, *FHL2*, *TECRL*, *NPPA*/*NPPB*; Fig 5i-q, Extended Data 17, 18, 19; FDR<0.05 for multiple comparisons). Thus, direct co-regulation of target genes by TBX5, MEF2c, and MEF2a, in addition to previously known interactions with NKX2-5 and GATA4, may be a potential TBX5 dosage-dependent mechanism for CHDs.

bioRxiv preprint doi: https://doi.org/10.1101/835603; this version posted November 10, 2019. The copyright holder for this preprint (which was not certified by peer review) is the author/funder, who has granted bioRxiv a license to display the preprint in perpetuity. It is made available under aCC-BY-ND 4.0 International license.

Discussion

Our studies with a human cellular model of CHD has defined consequences of reduced TBX5 dosage during cardiac differentiation at single cell resolution. Of potential relevance to a range of anatomical and functional manifestations of *TBX5* haploinsufficiency, we uncovered discrete responses to reduced TBX5 dosage in susceptible cardiomyocyte subtypes. The quantitative specificity of TBX5-dependent cell types underscores cellular complexity in response to transcription factor dosage. Analysis of human TBX5 dose-sensitive GRNs identified vulnerable nodes enriched for CHD-associated or cardiac development genes, suggesting a vital role for TBX5 dosage to maintain cardiac network stability. The sensitivity of a GRN to transcription factor dosage has been observed in *Drosophila* embryo patterning [35] for example, but has not been linked to human disease to date. The biophysical rules regulating transcription factor dosage sensitivity are only now becoming understood, and our results in a human CHD model may bring immediate pertinence of human disease to this biological context.

From TBX5-sensitive GRNs, we discovered several important nodes linking many CHD-related genes. For example, the reduced centrality of *MEF2C* in the TBX5-dependent GRN suggests an important and sensitive link between these cardiac transcription factors. Indeed, we validated this predicted genetic interaction in mouse, which yielded muscular VSDs, a type of CHD rarely observed in mouse models but common in humans. It is likely that other sensitive nodes in a TBX5-dependent network will illuminate novel aspects of CHD and cardiac gene regulation. Variability in CHDs with monogenic inherited or *de novo* mutations could be explained by additional mutations in genes that form part of these functional networks, as illuminated by our findings, and as evidenced by oligogenic inheritance of CHD-causing variants [11]. Our results point to a genomic framework that will guide genetic insights into the underpinnings of CHD.

bioRxiv preprint doi: https://doi.org/10.1101/835603; this version posted November 10, 2019. The copyright holder for this preprint (which was not certified by peer review) is the author/funder, who has granted bioRxiv a license to display the preprint in perpetuity. It is made available under aCC-BY-ND 4.0 International license.

Contributions. I.S.K. and B.G.B conceived and designed the project. B.I.G., L.W., L.B., T.S. and I.S.K. performed gene targeting and isolation of mutant iPSCs. B.I.G., K.S.R, P.G., T.S., and I.S.K. performed in vitro differentiation and harvested samples. P.G. performed the Western analysis. M.H.L. performed electrophysiology analyses. R.T. performed statistical analyses for electrophysiology. K.S.R. performed immunostaining and scoring of cardiomyocytes. G.A.A. performed RNAscope and flow cytometry. K.S.R. and I.S.K. performed Seurat analyses. K.S.R., A.P.B., H.G., and I.S.K. performed pseudotime analyses. H.G. implemented the cell browser. G.I. performed gene regulatory network analyses. W.P.D. and I.S.K. performed phenotype analyses of mutant mice. I.S.K. performed bulk RNAseq analyses. B.N.A., F.G., K.L., and W.T.P. performed ChIP-seq experiments and peak calling. S.K.H. and R.T. performed association analyses of co-occupancy, gene expression and disease candidates. J.M.S., W.T.P., C.E.S., J.G.S., and H.H. provided advisement. I.S.K. and B.G.B. wrote the manuscript, with comments and contributions from all authors.

Acknowledgements. We thank Dario Miguel-Perez and Sarah Wood for mouse genotyping and colony maintenance, Jeff Farrell for input on URD, David Joy and Todd McDevitt for sharing in-house imaging software, Brian Black for mouse lines, Kathryn Claiborn for editorial assistance, and members of the Bruneau lab for discussions and comments. We also thank the Gladstone Bioinformatics, Genomics, Histology and Microscopy, and Stem Cell Cores, R. Sarah Elmes at the UCSF Laboratory for Cell Analysis, the UCSF Center for Advanced Technology, the Salk Institutes Center of Excellence for Stem Cell Genomics, Matthew Speir and Maximilian Haeussler at cells.ucsc.edu, and the UCSC Stem Cell Data Center Hub for their invaluable assistance. This work was supported by grants from the National Institutes of Health (NHLBI Bench to Bassinet Program UM1HL098179 to B.G.B. and UM1HL098166 to J.G.S. and W.T.P., 2T32HL007731-27 to S.K.H), , the Foundation for Anesthesia Education and Research

bioRxiv preprint doi: https://doi.org/10.1101/835603; this version posted November 10, 2019. The copyright holder for this preprint (which was not certified by peer review) is the author/funder, who has granted bioRxiv a license to display the preprint in perpetuity. It is made available under aCC-BY-ND 4.0 International license.

(Mentored Research Training Grant to I.S.K.), Society for Pediatric Anesthesia (Young Investigator Award to I.S.K.), Hellman Family Fund (I.S.K.), UCSF REAC Grant (I.S.K.) and UCSF Department of Anesthesia and Perioperative Care (New Investigator Award to I.S.K.). H.H. is a Miguel Servet (CP14/00229) researcher supported by the Spanish Institute of Health Carlos III (ISCIII) and Ministerio de Ciencia, Innovación y Universidades (SAF2017-89109-P; AEI/FEDER, UE). This work was also supported by the California Institute for Regenerative Medicine (RB4-05901 to B.G.B), an NIH/NCRR grant (C06 RR018928) to the J. David Gladstone Institutes, the Younger Family Fund (B.G.B.), and the Office of the Assistant Secretary of Defense for Health Affairs through the Peer Review Medical Research Program under Award No. W81XWH-17-1-0191. Opinions, interpretations, conclusions and recommendations are those of the author and are not necessarily endorsed by the Department of Defense. In conducting research using animals, the investigator(s) adheres to the laws of the United States and regulations of the Department of Agriculture. In the conduct of research utilizing recombinant DNA, the investigator adhered to NIH Guidelines for research involving recombinant DNA molecules.

Competing Interests: B.G.B. is a co-founder and shareholder of Tenaya Therapeutics. None of the work presented here is related to the interests of Tenaya Therapeutics.

bioRxiv preprint doi: https://doi.org/10.1101/835603; this version posted November 10, 2019. The copyright holder for this preprint (which was not certified by peer review) is the author/funder, who has granted bioRxiv a license to display the preprint in perpetuity. It is made available under aCC-BY-ND 4.0 International license.

Methods

Gene targeting and genotyping of human iPS cells mutant for *TBX5*. sgRNAs for *TBX5* exon 3 (sgRNA1, TCCTTCTTGCAGGGCATGGA) or exon 7 (sgRNA2, CCTTTGCCAAAGGATTTCG), which encode the T-box domain, were selected using crispr.genome-engineering.org, and cloned by annealing pairs of oligos into a plasmid containing humanized *S. pyogenes* Cas9, as described in [36] (px330-U6-Chimeric_BB-CBh-hSpCas9 was a gift from Feng Zhang, Addgene #42230).

For WTC11-derivatives $TBX5^{+/+}$ (control), $TBX5^{in/+}$ or $TBX5^{in/del}$, the induced pluripotent stem (iPS) cell line WTC11 (gift from Bruce Conklin, available at NIGMS Human Genetic Cell Repository/Coriell #GM25236) [37] was electroporated (Lonza #VPH-5012) with a cloned nuclease construct containing a guide RNA (sgRNA1) targeting exon 3 of *TBX5*, as described in [37,38]. Cells were plated on human ESC-grade Matrigel (Corning #354277) and cultured in mTeSR-1 (StemCell Technologies Cat #05850) with 10μM ROCK inhibitor (StemCell Technologies, Y-27632). For screening of *TBX5* exon 3 non-homologous end-joining (NHEJ) mutations, genomic DNA flanking the targeted sequence was amplified by PCR (For1: ATGGCATCAGGCGTGTCCTATAA and Rev1: CCCACTTCGTGGAATTTTAGCCA), amplicons underwent digestion by NlaIII, and then evaluated for loss of NlaIII by gel electrophoresis (wildtype band 800bp, mutant band 880bp). Clones with no change, a heterozygous or homozygous loss of NlaIII were sequenced (For1: ATGGCATCAGGCGTGTCCTATAA, Rev1: TTCCGGGCTTGAACTTCTGG, Seq1: ATAGCCTTGTGCTGATGGCA).

For generation of $TBX5^{PuR/PuR}$, a puromycin resistance gene cassette (Frt-PGK-EM7-PuroR-bpA-Frt) containing homology arms of 469bp (5' homology arm) and 466bp (3' homology arm) around the sgRNA1 target site at +9bp from the start of *TBX5* exon 3 was cloned by Cold Fusion (System Biosciences #MC010B) using amplicons from genomic DNA of WTC11 into a construct that was a modification of plasmid pEN114[39]. WTC11 cells were

bioRxiv preprint doi: https://doi.org/10.1101/835603; this version posted November 10, 2019. The copyright holder for this preprint (which was not certified by peer review) is the author/funder, who has granted bioRxiv a license to display the preprint in perpetuity. It is made available under aCC-BY-ND 4.0 International license.

electroporated with a cloned nuclease construct containing a guide RNA targeting exon 3, along with the *TBX5* exon3 homology arm-Frt-PGK-EM7-PuroR-bpA-Frt cassette and plated as a serial dilution in mTeSR-1 with Rock inhibitor, as described in [38]. On day 2 and subsequent days, cells were grown in media containing mTeSR-1, Rock inhibitor and puromycin (0.5ug/mL), to select for puromycin-resistant cells. For screening of *TBX5* exon 3 homology-directed repair (HDR) mutations, genomic DNA flanking the targeted sequence was amplified by PCR (For1: ATGGCATCAGGCGTGTCCTATAA, and Rev2: CCCACTTCGTGGAATTTTAGCCA for wildtype, 797 bp, For1: ATGGCATCAGGCGTGTCCTATAA, Rev3: GTTCTTGCAGCTCGGTGAC [39] for PuroR, 1631 bp). Positive 5' arm clones were genotyped by PCR for the 3' arm (For2: ATTGCATCGCATTGTCTGAG [39], Rev4: TTTGACAATCGGGTGGGACC, 829 bp).

For PGP1-derivatives $TBX5^{in/+}$ or $TBX5^{del/del}$, the iPS cell line PGP1 (gift from George Church, available at NIGMS Human Genetic Cell Repository/Coriell #GM23338) [40] was electroporated with a cloned nuclease construct containing a guide RNA (sgRNA2) targeting exon 7 of *TBX5*, as described in [41]. For screening of *TBX5* exon 7 NHEJ mutations, the targeted sequence was amplified using PCR primers (For3: GCTTCTTTTGGTTGCCAGAG, Rev5: CATTCTCCCCATTTCCATGT, Seq2: AGAGGCTGCATTTCCATGAT), Illumina compatible-libraries from clones were generated and multiplex-sequenced on a MiSeq for purity of homogeneity of clones for heterozygous or homozygous mutations, as described in [41].

Isolation of homogenous iPS cell clones. Isolation of homogenous colonies for WTC11-derivatives $TBX5^{+/+}$ (control), $TBX5^{in/+}$ or $TBX5^{in/\mathrm{del}}$ was performed by modification of methods described previously [38,42]. Briefly, single cell suspension of electroporated iPS cells was plated on Matrigel-coated 6 well plates (WP) (BD Bioscience #351146). Once cultures were adherent and recovered to ~80% confluency, cells were detached by Accutase Cell Detachment Solution (Stemcell Technologies #07920), diluted with 1X DPBS without Ca^{2+}/Mg^{2+} and singularized

bioRxiv preprint doi: https://doi.org/10.1101/835603; this version posted November 10, 2019. The copyright holder for this preprint (which was not certified by peer review) is the author/funder, who has granted bioRxiv a license to display the preprint in perpetuity. It is made available under aCC-BY-ND 4.0 International license.

using a P1000 filtered tip, and centrifuged. The cell pellet was resuspended in mTeSR-1, Rock inhibitor and Gentamicin (Life Technologies #15750-060) media, incubated with DAPI (1:1000 from a 1mg/mL stock) for 5 min, centrifuged and resuspended at a concentration of at least 1.0E6 cells/mL in mTeSR-1, Rock inhibitor and Gentamicin media without DAPI. After filtering cells with a 40-micron mesh into FACS tubes, remaining cells (about 120,000 cells per well) were plated on to 6WP for maintenance. Single cells were then sorted for DAPI negativity using a BD FACS AriaII or AriaIII, with a 100-micron nozzle at the lowest flow rate available, into individual wells of a 96WP coated with Matrigel containing media of mTeSR-1, Rock inhibitor and Gentamicin. Upon recovery at 37°C, each well was evaluated one day later for no cells, one cell or more than one cell. All cells were maintained with mTeSR-1, Rock inhibitor and Gentamicin media for at least 5 days, then with mTeSR-1 alone for an additional 5-7 days. Each well at 25% confluency was harvested and re-plated upon singularization with P200 tips in 96WP for more efficient cell growth. When the cell confluency of each well from “single” cells was nearly 100%, then 90% of cells were harvested for genotyping using QuickExtract DNA lysis solution (Epicentre #QE0905T), while 10% of cells were re-plated for the next round of cell selection for wells of interest by FACS sorting again or by serial dilution of cells for manual picking of colonies, as described in [37,38] from apparent “single” cells. Rounds were repeated until every daughter well showed the same genotype, consistent with homogeneity. Genomic DNA from individual wells of interest were amplified using high fidelity *Taq* polymerase, TA-cloned and sequenced to confirm genotype and homogeneity.

Isolation of a homogenous colonies for PGP1-derivatives $TBX5^{in/+}$ or $TBX5^{del/del}$ was performed, as described in {Byrne:2007fn}. Isolation of a homogenous colonies for WTC11-derivative $TBX5^{PuR/PuR}$ was performed, as described in [38].

After sequencing confirmation of respective genotypes, karyotypically-normal cells from each iPS cell line were expanded for subsequent studies.

bioRxiv preprint doi: https://doi.org/10.1101/835603; this version posted November 10, 2019. The copyright holder for this preprint (which was not certified by peer review) is the author/funder, who has granted bioRxiv a license to display the preprint in perpetuity. It is made available under aCC-BY-ND 4.0 International license.

Maintenance of iPS cells and differentiation to cardiomyocytes. All iPS cell lines were transitioned to and maintained on growth factor-reduced basement membrane matrix Matrigel (Corning #356231) in mTeSR-1 medium. For directed cardiac differentiations, iPS cells were dissociated using Accutase and seeded on to 6WP or 12WP. The culture was allowed to reach 80-90% confluency and induced with the Stemdiff Cardiomyocyte Differentiation Kit (Stemcell Technologies #05010), according to the manufacturer's instructions. Starting on day 7, differentiations were monitored daily for beating cardiomyocytes and onset of beating was recorded as the day when beating was first observed.

Flow Cytometry. iPS-derived cardiomyocytes from WTC11, Control, *TBX5*$^{in/+}$ and *TBX5*$^{in/del}$ lines were dissociated using Trypsin-EDTA 0.25% on day 15 or day 23 after induction of the differentiation protocol and fixed with 4% methanol-free formaldehyde. Cells were washed with PBS and permeabilized using FACS buffer (0.5% w/v saponin, 4% Fetal Bovine Serum in PBS). For evaluation of differentiation efficiency, cells were stained with a mouse monoclonal antibody for cardiac isoform Ab-1 Troponin at 1:100 dilution (ThermoFisher Scientific #MS-295-P) or the isotype control antibody (ThermoFisher Scientific #14-4714-82). For analyzing levels of Desmin protein, cells were co-stained with the mouse monoclonal antibody for cardiac isoform Ab-1 Troponin at 1:100 dilution and recombinant rabbit anti-Desmin antibody at 1:70 dilution (Abcam #ab32362), or normal rabbit IgG antibody (Millipore Sigma #NI01) for 1 hour at room temperature. After washing with FACS buffer, cells were stained with the following secondary antibodies - goat anti-mouse IgG Alexa 594 at 1:200 dilution (ThermoFisher Scientific #A-11005) and donkey anti-rabbit IgG Alexa 488 at 1:200 dilution (ThermoFisher Scientific #A21206) for 1 hour at room temperature. Cells were then washed with FACS buffer, stained with DAPI for 5 minutes, rinsed, and filtered with a 40-micron mesh. At least 10,000 cells were analyzed using the BD FACSAriaII or AriaIII, and results were processed using FlowJo (BD Bioscience). Gating strategy is shown in Extended Data 20.

bioRxiv preprint doi: https://doi.org/10.1101/835603; this version posted November 10, 2019. The copyright holder for this preprint (which was not certified by peer review) is the author/funder, who has granted bioRxiv a license to display the preprint in perpetuity. It is made available under aCC-BY-ND 4.0 International license.

Western blotting. iPS-derived cardiomyocytes were harvested on day 15, pelleted and flash frozen. Protein was isolated from supernatant in RIPA buffer with EDTA-free protease and phosphatase inhibitor (ThermoFisher Scientific) after sonication (15 second pulse on, 15 second pulse off, for four pulses). After quantification by BCA assay (ThermoFisher Scientific), 150µg of total protein was loaded per well for each genotype. After running on SDS-PAGE and wet transfer with NuPage Transfer buffer (ThermoFisher Scientific) to a PVDF membrane, the blot was washed in PBST and incubated in primary antibodies of rabbit polyclonal anti-TBX5 at a 1:400 dilution (Sigma #HPA008786) and mouse monoclonal anti-cTNT at 1:1000 dilution (ThermoFisher Scientific #MS-295-P), followed by secondary antibody incubation with donkey anti-rabbit IgG IRDye680 at 1:2000 dilution (Licor #926-68073) and donkey anti-mouse IgG IRDye800 at 1:2000 dilution (Licor #926-32212). The blot was imaged on an Odyssey FC Dual-Mode Imaging system (Licor).

Fluorescent *in situ* hybridization. iPS cell-derived cardiomyocytes from WTC11, Control, *TBX5*$^{in/+}$,*TBX5*$^{in/del}$ and *TBX5*$^{PuR/PuR}$ were dissociated using Trypsin-EDTA 0.25% on day 23 after induction of the differentiation protocol, and 25,000-40,000 cells were plated on to 8-well chambered slides (Ibidi #80826), to obtain a relatively sparse monolayer of cardiomyocytes. Cells were fixed the following day with 10% Neutral Buffered Formalin for 15 minutes at room temperature. Cells were then serially dehydrated in 50%, 70% and 100% ethanol and stored at -20°C until ready to be hybridized. *In situ* hybridization was performed using the RNAscope Multiplex Fluorescent v2 Assay kit (Advanced Cell Diagnostics #323100) with probes for *Hs-TNNT2* (#518991) and *Hs-NPPA* (#531281). Slides were imaged at 10X and 40X magnification on the Keyence BZ-X710 All-in-One Fluorescence Microscope. Mean intensity of *NPPA* signal was measured in each *TNNT2*+ cell from every group. Unpaired t-tests were used to calculate statistical significance.

bioRxiv preprint doi: https://doi.org/10.1101/835603; this version posted November 10, 2019. The copyright holder for this preprint (which was not certified by peer review) is the author/funder, who has granted bioRxiv a license to display the preprint in perpetuity. It is made available under aCC-BY-ND 4.0 International license.

Replating cardiomyocytes for single cell electrophysiology. iPS cell-derived cardiomyocytes (day 15 or older) from WTC11, Control, *TBX5*$^{in/+}$, *TBX5*$^{in/del}$ and *TBX5*$^{PuR/PuR}$ were gently dissociated in Trypsin-EDTA 0.25% and quenched using StemDiff Maintenance Medium with 10% FBS. Cell suspension was centrifuged at 800 rpm for 5 minutes. The pellet was resuspended in StemDiff Maintenance Medium with Rock inhibitor at a 1:1000 dilution. Cardiomyocytes were counted, and 25,000-35,000 cells were plated on to growth factor-reduced Matrigel-coated 15mm round glass coverslips (Warner Instruments #64-0703) to obtain a sparse distribution. Cardiomyocytes were then maintained on coverslips in StemDiff Maintenance Medium.

Patch Clamp Electrophysiology. Patch clamp recordings were made on single iPSC-derived CMs using the perforated-patch configuration. Experiments were performed at 30°C under continuous perfusion of warmed Tyrode's solution containing (in mM): 140 NaCl, 5.4 KCl, 1 $CaCl_2$, 1 $MgCl_2$, 10 glucose, and 10 HEPES, with the pH adjusted to 7.4 with NaOH. Recordings were conducted using borosilicate glass pipettes (Sutter Instruments) with typical resistances of 2 to 4MΩ. The pipette solution consisted of (in mM): 150 KCl, 5 NaCl, 5 MgATP, 10 HEPES, 5 EGTA, 2 $CaCl_2$, and 240 μg/mL amphotericin B, with the pH adjusted to 7.2 with KOH. Spontaneous action potentials were acquired in a zero-current current clamp configuration using an Axopatch 200B amplifier and pClamp 10 software (Axon Instruments). Data was digitized at 20 kHz and filtered at 1kHz. Action potential parameters from each cell were derived using Clampfit 10 software (Axon Instruments).

Fluorescent recordings of calcium flux. iPSC-derived CMs on glass coverslips were loaded with Ca^{2+} indicator dye Fluo-4 AM (Thermo Fisher Scientific #F14201) to record Ca^{2+} flux, as

bioRxiv preprint doi: https://doi.org/10.1101/835603; this version posted November 10, 2019. The copyright holder for this preprint (which was not certified by peer review) is the author/funder, who has granted bioRxiv a license to display the preprint in perpetuity. It is made available under aCC-BY-ND 4.0 International license.

502 previously described [43]. Measurements were made on spontaneously firing single or small clusters of iPSC-derived CMs using a 10X objective on a Zeiss Axio Observer Z1 inverted
504 microscope. For experiments, cells were placed in Tyrode's solution containing 1.8 mM Ca^{2+} within a 37°C heated stage-top imaging chamber (Okolab). Images were acquired at 100 fps
506 using an ORCA-Flash 4.0 camera (Hamamatsu, Bridgewater, NJ). Data was processed using ZEN (Zeiss) or Image J software (http://rsbweb.nih.gov/ij/) and analyzed using custom in-house
508 software [44].

510 **Graphing and statistics for electrophysiology.** For electrophysiology and calcium imaging experiments, graphs were generated using Prism 8.2.0 (GraphPad Software). Significance
512 between parental and experimental groups was determined with a custom R-script using unpaired two-sided Welch's *t* tests with Holm-Sidak correction for multiple comparisons [12].
514 Adjusted $P < 0.05$ was considered statistically significant.

516 **Immunostaining and scoring of cardiomyocytes.** iPSC-derived cardiomyocytes from WTC11, Control, $TBX5^{in/+}$ and $TBX5^{in/del}$ were replated on coverslips placed in 12-well plates on
518 day 23, as described above for replating for electrophysiology. Cells were fixed in 4% formaldehyde for 20 minutes at room temperature, followed by washes in PBS. Cells were then
520 treated with a blocking buffer containing 5% goat serum and 0.1% Triton X-100 in PBS for 1 hour at room temperature. A mouse monoclonal antibody for cardiac isoform Ab-1
522 Troponin (ThermoFisher Scientific #MS-295-P) was added to the coverslip-containing wells at a 1:100 dilution in blocking buffer and incubated on a rocker for 2 hours at room temperature.
524 Following washes with 0.1% Triton X-100 in PBS, coverslips were treated with a donkey anti-rabbit IgG Alexa 488 antibody (ThermoFisher Scientific #A21206) at a 1:200 dilution for 2 hours
526 at room temperature. Coverslips were then washed with 0.1% Triton X-100 in PBS and stained

bioRxiv preprint doi: https://doi.org/10.1101/835603; this version posted November 10, 2019. The copyright holder for this preprint (which was not certified by peer review) is the author/funder, who has granted bioRxiv a license to display the preprint in perpetuity. It is made available under aCC-BY-ND 4.0 International license.

with DAPI at a 1:1000 dilution for 2 minutes. Coverslips were washed and stored in PBS at 4C. Images were acquired on a Zeiss LSM 880 with Airyscan and processed by ImageJ [45].

Myofibrillar arrangement in cardiomyocytes was manually scored on a scale of 1-5, similar to [46]. A score of 1 represents cells with intact myofibrils in a parallel arrangement. A score of 2 represents cells that have intact myofibrils, but many are not parallel. Scores of 3 and of 4 include cells with increasing degrees of myofibrillar fragmentation or aggregation. A score of 5 represents cells without visible myofibrils. No cells were apparent among our samples with a score of 5. Violin plots were generated in Prism (GraphPad) to show distribution of scored cells from each group. Fisher's exact test was used to determine statistical significance.

Cell harvesting for single cell RNAseq. Cells from day 6, day 11 or day 23 of the differentiation protocol were collected from 3 independent differentiations. Wells for dissociation were chosen based on typical differentiated morphology on day 6 or robust beating on day 11 and day 23. Cells were singularized with Trypsin-EDTA 0.25%. After quenching, the single cell suspension was centrifuged at 800 rpm for 5 minutes. The pellet was resuspended in 1X PBS with 0.04% w/v Ultrapure BSA (MCLAB #UBSA-500) and counted. A 30μL cell suspension containing 10,000 cells was used to generate single cell droplet libraries with the Chromium Single Cell 3′ GEM, Library & Gel Bead Kit v2 according to manufacturer's instructions (10X Genomics). After KAPA qPCR quantification, a shallow sequencing run was performed on a NextSeq 500 (Illumina) prior to deep sequencing on a NextSeq 500, HiSeq 4000, or NovaSeq (Illumina) for a read depth of >100 million reads per cell.

Data processing using Cellranger. All datasets were processed using Cellranger 2.0.2. FASTQ files were generated using the mkfastq function. Reads were aligned to hg19 reference (version 1.2.0). Cellranger aggr was used to aggregate multiple GEM libraries.

bioRxiv preprint doi: https://doi.org/10.1101/835603; this version posted November 10, 2019. The copyright holder for this preprint (which was not certified by peer review) is the author/funder, who has granted bioRxiv a license to display the preprint in perpetuity. It is made available under aCC-BY-ND 4.0 International license.

Seurat analysis. Outputs from the Cellranger pipeline were analyzed using the Seurat package (version 2.3.4) in R (version 3.5.1) [R Core Team (2018). R: A language and environment for statistical computing. R Foundation for Statistical Computing, Vienna, Austria. URL https://www.R-project.org/]. Datasets from day 6, day 11 or day 23 experiments were analyzed as separate Seurat objects. Quality control steps were performed to remove dead cells or doublets, and cells with a UMI count between 10,000 to 80,000 were retained. After normalizing the data, sources of unwanted variation, such as differences in the number of UMI, number of genes, percentage of mitochondrial reads and differences between G2M and S phase scores were regressed using the ScaleData function. Next, principal component analysis (PCA) was performed using the most highly variable genes. Cells were then clustered based on the top 25-30 principal components and visualized using a dimensionality reduction method called Uniform Manifold Approximation and Projection (UMAP) [47]. The resolution parameter was set, so that cluster boundaries separated the major cell types.

For day 11 or day 23 cardiomyocyte datasets, *TNNT2*$^{+}$ clusters were defined as containing a majority of cells expressing *TNNT2* on a feature plot and extracted using the SubsetData function and re-clustered. Subsequently, the resolution parameter was set to partition clusters enriched for a particular genotype. A phylogenetic tree was generated by relating the “average” cell from each cluster by centroid analysis, using the BuildClusterTree function. Differential gene expression tests were run between closely related clusters, using the FindMarkers function with min.pct set to 0.1 and logfc.threshold set to 0.25. Selected differentially expressed genes with an adjusted p-value less than 0.05 from the Wilcoxon Rank Sum test were then displayed using the Dotplot function. As Seurat log normalizes gene expression counts and scales values for each gene (mean is 0, std dev of +/-1), dot plots and heatmaps are based on scaled expression values.

Major cell type categories were defined by their expression of certain marker genes - cardiomyocytes (*TNNT2*), dividing cardiomyocytes (*CENPF*+*TNNT2*), fibroblasts (*COL1A1*),

bioRxiv preprint doi: https://doi.org/10.1101/835603; this version posted November 10, 2019. The copyright holder for this preprint (which was not certified by peer review) is the author/funder, who has granted bioRxiv a license to display the preprint in perpetuity. It is made available under aCC-BY-ND 4.0 International license.

endoderm (*TTR* alone or *TTR+AFP*) and endothelial cells (*PLVAP*). Clusters of cells not defined by any of these markers were labeled as 'Others'. The numbers of cells in each major cell type category in each genotype were then calculated. Sunburst plot was generated in Excel using the percentage of cells in each cell type category per genotype. We used FindAllMarkers to generate a list of top marker genes for each cluster and presented two selected genes in a dot plot to display potential diversity of subtypes among these major cell types.

Congenital Heart Disease-Associated or Electrophysiology-Related Gene Lists and Cell-Type Expression. A list of 376 CHD-associated candidate genes were manually curated from [18-25], including inherited, *de novo*, syndromic or non-syndromic CHD-associated genes. A list of 76 EP-linked genes were manually curated. A list of cardiac development-related factors is from [48]. Lists can be found in Supplementary Table 1.

To determine cell-type enrichment of each CHD-associated gene, cells in the day 23 dataset were assigned one of five cell-type labels (cardiomyocytes, fibroblasts, endoderm, endothelial and others). A dot plot was generated to visualize the expression of CHD-associated genes in the 5 cell types. Genes were first manually curated for enrichment in a certain cell type, based on expression. Statistical significance of the enrichment of a certain gene in one cell type over the others was then evaluated by Wilcoxon Rank Sum test (adjusted p-value < 0.05).

Cell trajectories and pseudotime analysis. Pseudotime analysis was performed using the URD package (version 1.0.2). A single Seurat object with data from three timepoints and four genotypes was processed, as described in the previous section, and then converted to an URD object using the seuratToURD function. Cell-to-cell transition probabilities were constructed, by setting the number of nearest neighbors (knn) to 211 and sigma to 8. Pseudotime was then calculated by running 80 flood simulations with *POU5F1+* clusters as the 'root' cells. Next, all

bioRxiv preprint doi: https://doi.org/10.1101/835603; this version posted November 10, 2019. The copyright holder for this preprint (which was not certified by peer review) is the author/funder, who has granted bioRxiv a license to display the preprint in perpetuity. It is made available under aCC-BY-ND 4.0 International license.

day 23 clusters were set as 'tip' cells and biased random walks were simulated from each tip to build an URD tree.

To identify genes that correlate with pseudotime in one genotype but not the other, we calculated Spearman rank correlation, using Python (v3.7.3, and libraries Pandas 0.25.0, Numpy 1.17.1, and SciPy 1.3.1), to find genes that share a significant monotonic relationship (p-value less than 0.05) with pseudotime. To determine if these monotonic relationships differ between WT and *TBX5*$^{in/del}$ paths to cardiomyocytes, we used a Fisher z-transformation to test the null hypothesis that there is no significant difference in correlation [49]. To illustrate these results, we use a scatter plot for all genes with a significant rho value (p-value<0.05 by two-sided *t* test), or heat maps for genes with a |rho|≥0.4 to pseudotime and Z-score≥15 as a difference between WT and *TBX5*$^{in/del}$ paths.ki

To identify differential expressed genes in inferred cardiac precursors (stems in the URD tree) that are affected by *TBX5* loss, cell barcodes from each precursor segment (69 for wildtype/control/*TBX5*$^{in/+}$ path and 70 for *TBX5*$^{in/del}$ path) were extracted from the URD object and assigned new identities in the corresponding Seurat object. Differential gene test was then performed between the two segments using Wilcoxon Rank Sum test with min.pct set to 0.1 and logfc.threshold set to 0.25. Selected genes with an adjusted p-value less than 0.05 were plotted on the URD tree to visualize their expression.

To compare the trident (*TNNT2*$^{+}$ distal branch for WTC11, control and *TBX5*$^{in/+}$) and fork (*TNNT2*$^{+}$ distal branch for *TBX5*$^{in/del}$) during pseudotime, we subdivided the pseudotime from the common branchpoint to the tips of the trident and fork into twenty uniform windows. Within each window, we then calculated the t-test, difference of means, and fold change between the trident and fork for all genes. We filtered the statistics by gene-window combinations with p<0.05 after Bonferroni-Holm multiple testing correction. Then, we hierarchically clustered the genes on t-test p-values and plotted statistics using the R pheatmap library.

bioRxiv preprint doi: https://doi.org/10.1101/835603; this version posted November 10, 2019. The copyright holder for this preprint (which was not certified by peer review) is the author/funder, who has granted bioRxiv a license to display the preprint in perpetuity. It is made available under aCC-BY-ND 4.0 International license.

Gene ontology analysis. Gene ontology analysis was performed using 2018 biological process terms from org.Hs.eg.db (v3.8.2) and clusterProfiler (v 3.12.0), with a significance threshold set at p-value<0.05. To prevent high false discovery rate (FDR) in multiple testing, we used the default cutoff for the estimated q-value<0.05. Figures were produced using Matplotlib (v3.1.0). Gene ratios indicate the number of differentially expressed genes that overlap with each GO term divided by the total number of differentially expressed genes. For comparing *TNNT2*$^{+}$ clusters at d23, enriched gene ontology (GO) terms were determined using genes computed from a one-versus rest differential test (logfc>0.25; adj p-value<0.05 by Wilcoxon Rank Sum test) among clusters that were predominantly composed of the same *TBX5* genotype (WT-21, 12, 3, and Control-4, or *TBX5*$^{in/+}$- 9, 7, 6, and 0). Enriched GO terms associated with pseudotime in a WT- or *TBX5*$^{in/del}$ path were generated using genes positively correlated with pseudotime (rho≥|0.4|, and Z-score≥15) from each path. Several significant GO terms are highlighted.

Cell browser implementation. The cell browser at cells.ucsc.edu was developed by Maximilian Haeussler. We created a cell browser session that allows the user to interrogate the spatial distribution of metadata and expression across data, in multiple reduced dimensionality spaces including the URD trajectory. Using a Scanpy python pipeline, we generated PCA, tSNE, UMAP, PAGA, and drl transforms. We also imported the URD trajectory mapping and WGCNA transform from their respective packages. We ran the scoreCT algorithm to assign cell types to cell clusters using a marker gene set.

Gene regulatory network analysis. bigSCale2 (https://github.com/iaconogi/bigSCale2) [30] was used with default parameters to infer gene regulatory networks and “correlomes” from single cell RNAseq expression data for *TNNT2*$^{+}$ cells, simply passing as input expression counts and gene names. Details of each data set can be found in Supplementary Table 3. To evaluate significant

bioRxiv preprint doi: https://doi.org/10.1101/835603; this version posted November 10, 2019. The copyright holder for this preprint (which was not certified by peer review) is the author/funder, who has granted bioRxiv a license to display the preprint in perpetuity. It is made available under aCC-BY-ND 4.0 International license.

changes in pagerank (or degree) centrality, we computed all pairwise differential differences in pagerank (or degree) between baseline (wildtype or control) and *TBX5* mutants (*TBX5*$^{in/+}$ or *TBX5*$^{in/del}$) (12 total differences, from 2 *TBX5* mutants * 2 baselines * 3 stages) and used these values to determine the top 5% upper change cutoff from 8,704 genes of all networks. Classification of Pearson correlations were empirically chosen at >0.5 for correlation and <-0.05 for anti-correlation.

Mice. All mouse protocols were approved by the Institutional Animal Care and Use Committee at UCSF. *Tbx5*$^{del/+}$ [7] and *Tbx5*^{CreERT2IRES2xFLAG} (abbreviated here as *Tbx5*^{CreERT2}) [33] mice were described previously. *Tbx5*$^{fl\text{-}bio/fl\text{-}bio}$[50] mice were obtained from Frank Conlon. *Mef2c*$^{del/+}$ mice [32] were obtained from Brian Black. *Mef2a*$^{fl\text{-}bio}$ and *Mef2c*$^{fl\text{-}bio}$ (Jackson #025983) were described in [34]. *Rosa26BirA* mice were obtained from Jackson labs (Jackson #010920) [51].

ChIP-seq. Combined peaks of human TBX5 or GATA4 ChIP-seq from hiPSC-derived CMs were used [10]. bioChIP-seq of mouse TBX5, MEF2c and MEF2a from E12.5 hearts were from [34]. Single replicates of TF bioChIP peaks, which were IDR normalized (IDR_THRESHOLD=0.05 between each set of replicates), were defined as the summit of the peak with the strongest ChIP signal ± 100bp of the individual replicate with the greatest peak intensity. Mouse H3K27ac ChIP-seq at E12.5 of embryonic cardiac ventricles was from [52].

Bulk RNAseq analysis of embryonic mouse hearts. Embryos at E10.5 from timed matings of *Tbx5*$^{del/+}$ x *Tbx5*$^{CreERT2/+}$ were harvested. Each whole heart was dissected, placed in Qiazol, and homogenized with a 25-guage needle. Total RNA was extracted using the miRNeasy micro kit with on-column DNAse digestion (Qiagen) and assessed by bioanalyzer (Agilent) for RNA integrity, as previously described [53]. Four individual hearts of each genotype (wildtype, *Tbx5*$^{CreERT2/+}$, *Tbx5*$^{del/+}$ or *Tbx5*$^{del/CreERT2}$) from multiple litters were used as biological quadruplicates. RNAseq libraries were generated using the Ovation RNA-seq system V2 kit

bioRxiv preprint doi: https://doi.org/10.1101/835603; this version posted November 10, 2019. The copyright holder for this preprint (which was not certified by peer review) is the author/funder, who has granted bioRxiv a license to display the preprint in perpetuity. It is made available under aCC-BY-ND 4.0 International license.

(NuGen), and SPIA-amplified cDNA was made using the Ovation Ultralow System V2 kit (NuGen). Libraries were evaluated by bioanalyzer (Agilent), quantified using KAPA qPCR (Kapa Biosystems), and sequenced by paired-end 100 bp reads using a HiSeq2500 (Illumina), for a sequencing depth of >40 million reads per library. Reads were aligned to mm9 by TopHat2 [54] and counts per gene were tallied by featureCounts [55]. Differentially expressed genes were identified by EdgeR[56], using cutoffs of log2 fold-change of >0.5 or <-0.5, and raw p-value <0.01. R functions, K-means clustering and pheatmap, were used to cluster and create bulk RNAseq heatmaps.

Statistical analyses for correlations. We evaluated the pair-wise association among 24 variables, including all human genes, TBX5-dysregulated genes in cardiomyocytes from two different stages of differentiation (d11 or d23), CHD-associated genes, EP-linked genes, TBX5 or GATA4 binding [10], and genome-wide association (GWAS) genes for CHDs or arrhythmias. Reported GWAS genes from https://www.ebi.ac.uk/gwas/ for the terms congenital heart disease, congenital heart malformation, congenital left sided heart lesions, conotruncal heart defect and aortic coarctation were used to define congenital heart disease-related (CHD) GWAS genes. Reported genes from terms such as cardiac arrhythmia, supraventricular ectopy, ventricular ectopy, premature cardiac contractions, atrial fibrillation, sudden cardiac arrest and ventricular fibrillation were considered as arrhythmia-related (EP-GWAS) genes. Two nearest genes within 100kb, by using GREAT (great.stanford.edu), of TBX5 or GATA4 binding sites or of reported genes from each group of GWAS were considered for the analysis. The natural logarithm odds of genes associating with each one of these variables versus the odds of genes associating with every other variable were estimated using generalized linear models with family="binomial" setting in R. The resulting significances of these natural log odds ratios were adjusted for multiple testing by the Benjamini-Hochberg method [57]. Significance was determined using an FDR threshold of 0.05 or less.

bioRxiv preprint doi: https://doi.org/10.1101/835603; this version posted November 10, 2019. The copyright holder for this preprint (which was not certified by peer review) is the author/funder, who has granted bioRxiv a license to display the preprint in perpetuity. It is made available under aCC-BY-ND 4.0 International license.

Additional correlations were evaluated between 42 variables, including all mouse genes, mouse TBX5-dysregulated genes (from bulk RNAseq of E10.5 hearts from wildtype, *Tbx5*$^{del/+}$, *Tbx5*$^{CreERT2/+}$ or *Tbx5*$^{CreERT2/del}$ embryos), human TBX5-dysregulated genes from d11 or d23 cardiomyocytes, and TBX5, MEF2c or MEF2a binding sites from E12.5 mouse heart tissue [34]. Human gene symbols were converted to mouse gene symbols, using the getLDS() function from the biomaRt package (https://www.r-bloggers.com/converting-mouse-to-human-gene-names-with-biomart-package/). Two nearest genes within 100kb of TBX5, MEF2c or MEF2a binding sites were considered for the analysis.

For assessment of associations between binding locations of TBX5, MEF2c and MEF2a transcription factors with genes dysregulated by TBX5, analyses were performed corresponding to binding regions of each of the three TFs. First, binding regions of each TF was evaluated for association with genes, defined by nearest two genes within 100kb. Using the list of TBX5-dysregulated genes (mouse or human), binding regions of each TF associated with a TBX5-dysregulated gene was determined. Identified binding regions of each TF that overlapped with at least 50% of the binding regions of each of the other two TFs was determined, using bedops --element-of -50%. This approach defined three variables, including every binding region of the TF, if associated with a TBX5-dysregulated gene, or if it overlaps by at least 50% with the binding region of the other TFs, that were used for logistic regression in R. The resulting changes in odds are represented as natural logarithm odds ratios. Multiple testing correction was performed using the multtest package in R. All estimates are based on analyses for a given species (mouse or human TBX5-dysregulated).

Data availability. scRNAseq and bulk RNAseq datasets have been deposited at NCBI GEO, under accession GSE137876.

Code availability. R and python scripts will be available upon publication.

bioRxiv preprint doi: https://doi.org/10.1101/835603; this version posted November 10, 2019. The copyright holder for this preprint (which was not certified by peer review) is the author/funder, who has granted bioRxiv a license to display the preprint in perpetuity. It is made available under aCC-BY-ND 4.0 International license.

References.

1. Zaidi, S. & Brueckner, M. Genetics and Genomics of Congenital Heart Disease. *Circ Res* **120,** 923–940 (2017).

2. Hill, J. T., Demarest, B., Gorsi, B., Smith, M. & Yost, H. J. Heart morphogenesis gene regulatory networks revealed by temporal expression analysis. *Development* **144,** 3487–3498 (2017).

3. Hoffman, J. I. Incidence of congenital heart disease: II. Prenatal incidence. *Pediatr Cardiol* **16,** 155–165 (1995).

4. Hoffman, J. I. E. & Kaplan, S. The incidence of congenital heart disease. *J Am Coll Cardiol* **39,** 1890–1900 (2002).

5. Basson, C. T. *et al.* Mutations in human TBX5 [corrected] cause limb and cardiac malformation in Holt-Oram syndrome. *Nat Genet* **15,** 30–35 (1997).

6. Li, Q. Y. *et al.* Holt-Oram syndrome is caused by mutations in TBX5, a member of the Brachyury (T) gene family. *Nat Genet* **15,** 21–29 (1997).

7. Bruneau, B. G. *et al.* A murine model of Holt-Oram syndrome defines roles of the T-box transcription factor Tbx5 in cardiogenesis and disease. **106,** 709–721 (2001).

8. Mori, A. D. *et al.* Tbx5-dependent rheostatic control of cardiac gene expression and morphogenesis. **297,** 566–586 (2006).

9. Theodoris, C. V. *et al.* Human disease modeling reveals integrated transcriptional and epigenetic mechanisms of NOTCH1 haploinsufficiency. *Cell* **160,** 1072–1086 (2015).

10. Ang, Y.-S. *et al.* Disease Model of GATA4 Mutation Reveals Transcription Factor Cooperativity in Human Cardiogenesis. *Cell* **167,** 1734–1749.e22 (2016).

11. Gifford, C. A. *et al.* Oligogenic inheritance of a human heart disease involving a genetic modifier. *Science* **364,** 865–870 (2019).

bioRxiv preprint doi: https://doi.org/10.1101/835603; this version posted November 10, 2019. The copyright holder for this preprint (which was not certified by peer review) is the author/funder, who has granted bioRxiv a license to display the preprint in perpetuity. It is made available under aCC-BY-ND 4.0 International license.

12. Holm, S. A simple sequentially rejective multiple test procedure. *Scandinavian Journal of Statistics* **6,** 65–70 (1979).

13. Karakikes, I. *et al.* A Comprehensive TALEN-Based Knockout Library for Generating Human-Induced Pluripotent Stem Cell-Based Models for Cardiovascular Diseases. *Circ Res* **120,** 1561–1571 (2017).

14. Nadadur, R. D. *et al.* Pitx2 modulates a Tbx5-dependent gene regulatory network to maintain atrial rhythm. *Science Translational Medicine* **8,** 354ra115–354ra115 (2016).

15. Dai, W. *et al.* A calcium transport mechanism for atrial fibrillation in Tbx5-mutant mice. *eLife* **8,** 40 (2019).

16. Laforest, B. *et al.* Atrial fibrillation risk loci interact to modulate Ca2+-dependent atrial rhythm homeostasis. *J Clin Invest* **412,** 1825–15 (2019).

17. Zhu, Y. *et al.* Tbx5-dependent pathway regulating diastolic function in congenital heart disease. *Proceedings of the National Academy of Sciences* **105,** 5519–5524 (2008).

18. McCulley, D. J. & Black, B. L. Transcription factor pathways and congenital heart disease. *Curr. Top. Dev. Biol.* **100,** 253–277 (2012).

19. Zaidi, S. *et al.* De novo mutations in histone-modifying genes in congenital heart disease. **498,** 220–223 (2013).

20. Prendiville, T., Jay, P. Y. & Pu, W. T. Insights into the genetic structure of congenital heart disease from human and murine studies on monogenic disorders. *Cold Spring Harb Perspect Med* **4,** a013946–a013946 (2014).

21. Lalani, S. R. & Belmont, J. W. Genetic basis of congenital cardiovascular malformations. *Eur J Med Genet* **57,** 402–413 (2014).

bioRxiv preprint doi: https://doi.org/10.1101/835603; this version posted November 10, 2019. The copyright holder for this preprint (which was not certified by peer review) is the author/funder, who has granted bioRxiv a license to display the preprint in perpetuity. It is made available under aCC-BY-ND 4.0 International license.

22. Homsy, J. *et al.* De novo mutations in congenital heart disease with neurodevelopmental and other congenital anomalies. *Science* **350,** 1262–1266 (2015).

23. Sifrim, A. *et al.* Distinct genetic architectures for syndromic and nonsyndromic congenital heart defects identified by exome sequencing. *Nat Genet* **48,** 1060–1065 (2016).

24. Priest, J. R. *et al.* De Novo and Rare Variants at Multiple Loci Support the Oligogenic Origins of Atrioventricular Septal Heart Defects. *PLoS Genet* **12,** e1005963–25 (2016).

25. Jin, S. C. *et al.* Contribution of rare inherited and de novo variants in 2,871 congenital heart disease probands. *Nat Genet* **49,** 1593–1601 (2017).

26. Farrell, J. A. *et al.* Single-cell reconstruction of developmental trajectories during zebrafish embryogenesis. *Science* **108,** eaar3131–9 (2018).

27. Hiroi, Y. *et al.* Tbx5 associates with Nkx2-5 and synergistically promotes cardiomyocyte differentiation. *Nat Genet* **28,** 276–280 (2001).

28. Luna-Zurita, L. *et al.* Complex Interdependence Regulates Heterotypic Transcription Factor Distribution and Coordinates Cardiogenesis. *Cell* **164,** 999–1014 (2016).

29. Garg, V. *et al.* GATA4 mutations cause human congenital heart defects and reveal an interaction with TBX5. **424,** 443–447 (2003).

30. Iacono, G., Massoni-Badosa, R. & Heyn, H. Single-cell transcriptomics unveils gene regulatory network plasticity. 1–20 (2019). doi:10.1186/s13059-019-1713-4

31. Brin, S. & Page, L. The anatomy of a large-scale hypertextual Web search engine. *Computer Networks and Isdn Systems* **30,** 107–117 (1998).

bioRxiv preprint doi: https://doi.org/10.1101/835603; this version posted November 10, 2019. The copyright holder for this preprint (which was not certified by peer review) is the author/funder, who has granted bioRxiv a license to display the preprint in perpetuity. It is made available under aCC-BY-ND 4.0 International license.

32. Lin, Q., Schwarz, J., Bucana, C. & Olson, E. N. Control of mouse cardiac morphogenesis and myogenesis by transcription factor MEF2C. *Science* **276,** 1404–1407 (1997).

33. Devine, W. P., Wythe, J. D., George, M., Koshiba-Takeuchi, K. & Bruneau, B. G. Early patterning and specification of cardiac progenitors in gastrulating mesoderm. *eLife* **3,** (2014).

34. Akerberg, B. N. *et al.* A reference map of murine cardiac transcription factor chromatin occupancy identifies dynamic and conserved enhancers. *Nat Commun* **10,** 4907 (2019).

35. Stathopoulos, A. & Levine, M. Dorsal Gradient Networks in the Drosophila Embryo. **246,** 57–67 (2002).

36. Cong, L. *et al.* Multiplex Genome Engineering Using CRISPR/Cas Systems. *Science* **339,** 819–823 (2013).

37. Miyaoka, Y. *et al.* Isolation of single-base genome-edited human iPS cells without antibiotic selection. *Nat Meth* **11,** 291–293 (2014).

38. Mandegar, M. A. *et al.* CRISPR Interference Efficiently Induces Specific and Reversible Gene Silencing in Human iPSCs. *Stem Cell* **18,** 541–553 (2016).

39. Nora, E. P. *et al.* Targeted Degradation of CTCF Decouples Local Insulation of Chromosome Domains from Genomic Compartmentalization. *Cell* **169,** 930–933.e22 (2017).

40. Lee, J.-H. *et al.* A Robust Approach to Identifying Tissue-Specific Gene Expression Regulatory Variants Using Personalized Human Induced Pluripotent Stem Cells. *PLoS Genet* **5,** e1000718–15 (2009).

41. Byrne, S. M. & Church, G. M. Crispr-mediated Gene Targeting of Human Induced Pluripotent Stem Cells. *Current protocols in stem cell biology* **35,** 5A.8.1–22 (2015).

bioRxiv preprint doi: https://doi.org/10.1101/835603; this version posted November 10, 2019. The copyright holder for this preprint (which was not certified by peer review) is the author/funder, who has granted bioRxiv a license to display the preprint in perpetuity. It is made available under aCC-BY-ND 4.0 International license.

42. Peters, D. T., Cowan, C. A. & Musunuru, K. *Genome editing in human pluripotent stem cells*. (Harvard Stem Cell Institute, 2008).

43. Spencer, C. I. *et al.* Calcium Transients Closely Reflect Prolonged Action Potentials in iPSC Models of Inherited Cardiac Arrhythmia. *Stem Cell Reports* 1–13 (2014). doi:10.1016/j.stemcr.2014.06.003

44. Hookway, T. A. *et al.* Phenotypic Variation Between Stromal Cells Differentially Impacts Engineered Cardiac Tissue Function. *Tissue Engineering Part A* **25,** 773–785 (2019).

45. Abràmoff, M. D., Magalhães, P. J. & Ram, S. J. *Image processing with ImageJ.* 36–42 (Biophotonics International, 2004).

46. Judge, L. M. *et al.* A BAG3 chaperone complex maintains cardiomyocyte function during proteotoxic stress. *JCI Insight* **2,** 83–18 (2017).

47. Becht, E. *et al.* Dimensionality reduction for visualizing single-cell data using UMAP. *Nat Biotechnol* **37,** 38–44 (2018).

48. Duan, J. *et al.* Rational Reprogramming of Cellular States by Combinatorial Perturbation. *CellReports* **27,** 3486–3499.e6 (2019).

49. Fisher, R. A. On the‘ Probable Error’ of a Coefficient of Correlation Deduced from a Small Sample. *Metron* **1,** 3–32 (1921).

50. Waldron, L. *et al.* The Cardiac TBX5 Interactome Reveals a Chromatin Remodeling Network Essential for Cardiac Septation. *Dev Cell* **36,** 262–275 (2016).

51. Driegen, S. *et al.* A generic tool for biotinylation of tagged proteins in transgenic mice. *Transgenic Res* **14,** 477–482 (2005).

52. He, A. *et al.* Dynamic GATA4 enhancers shape the chromatin landscape central to heart development and disease. *Nat Commun* **5,** 4907 (2014).

bioRxiv preprint doi: https://doi.org/10.1101/835603; this version posted November 10, 2019. The copyright holder for this preprint (which was not certified by peer review) is the author/funder, who has granted bioRxiv a license to display the preprint in perpetuity. It is made available under aCC-BY-ND 4.0 International license.

53. Hota, S. K. *et al.* Dynamic BAF chromatin remodeling complex subunit inclusion promotes temporally distinct gene expression programs in cardiogenesis. *Development* **146,** dev174086–21 (2019).

54. Kim, D. *et al.* TopHat2: accurate alignment of transcriptomes in the presence of insertions, deletions and gene fusions. *Genome Biol* **14,** R36–13 (2013).

55. Liao, Y., Smyth, G. K. & Shi, W. featureCounts: an efficient general purpose program for assigning sequence reads to genomic features. *Bioinformatics* **30,** 923–930 (2014).

56. Robinson, M. D., McCarthy, D. J. & Smyth, G. K. edgeR: a Bioconductor package for differential expression analysis of digital gene expression data. *Bioinformatics* **26,** 139–140 (2009).

57. Benjamini, Y. & Hochberg, Y. Controlling the False Discovery Rate - a Practical and Powerful Approach to Multiple Testing. *Journal of the Royal Statistical Society Series B-Statistical Methodology* **57,** 289–300 (1995).

bioRxiv preprint doi: https://doi.org/10.1101/835603; this version posted November 10, 2019. The copyright holder for this preprint (which was not certified by peer review) is the author/funder, who has granted bioRxiv a license to display the preprint in perpetuity. It is made available under aCC-BY-ND 4.0 International license.

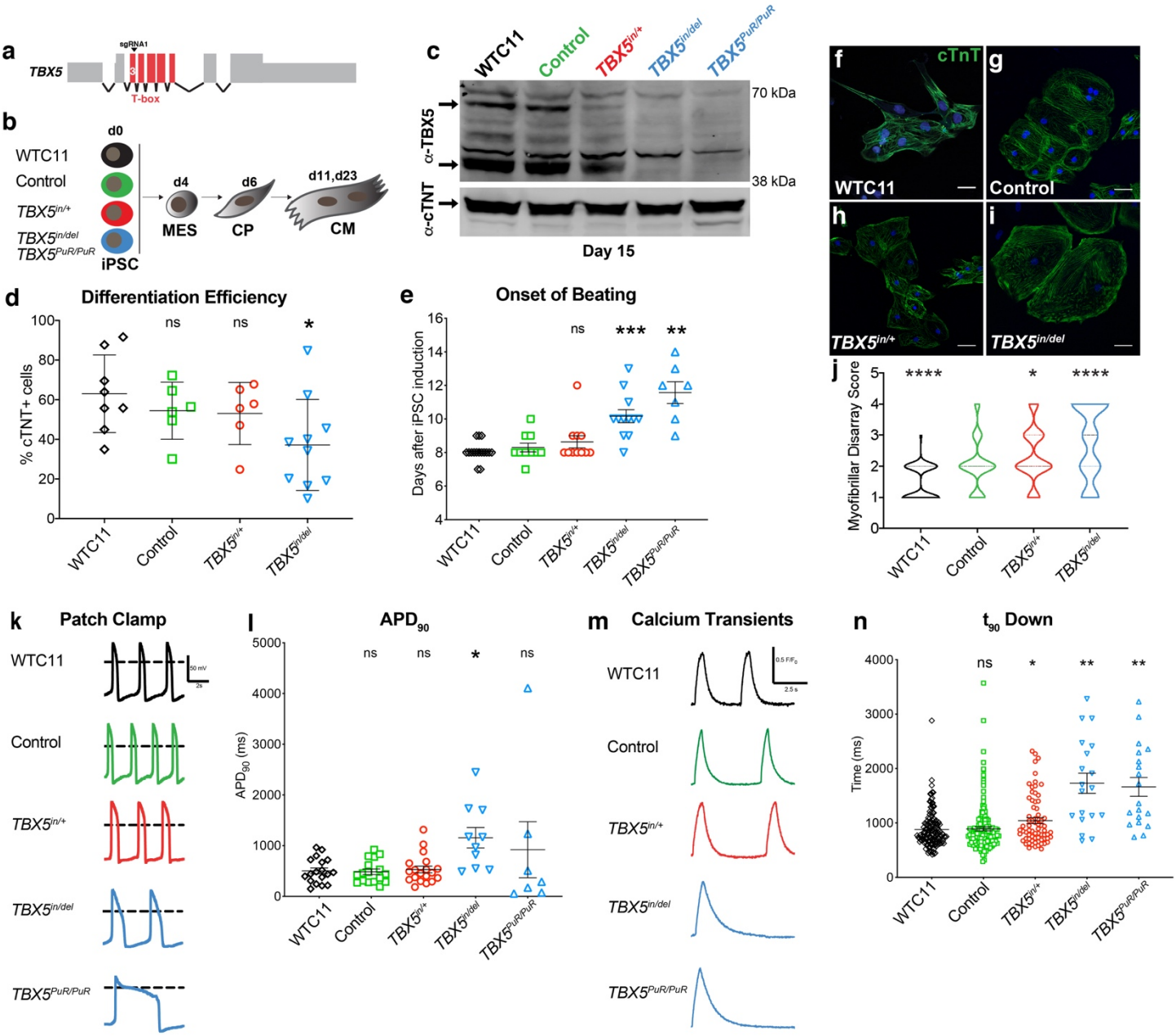

Figure 1. A human allelic series of *TBX5* mutants models features of congenital heart disease. a, Diagram of the human *TBX5* gene. Exons encoding the T-box domain of TBX5 are indicated in red. sgRNA1 was used to target exon 3 of *TBX5* by a CRISPR/Cas9 nuclease. **b**, Parental iPS cell line WTC11, control (CRISPR-treated, unmodified at exon 3 of *TBX5*) and targeted *TBX5* loss-of-function mutants (*TBX5*$^{in/+}$, *TBX5*$^{in/del}$, or *TBX5*$^{PuR/PuR}$) underwent directed differentiation to cardiomyocytes (CM) via mesoderm (MES) and cardiac precursor (CP) stages. **c**, TBX5 and cTNT protein expression for each *TBX5* genotype at day 15 (CMs). **d**, Differentiation efficiency by flow cytometry for cTNT^{+} cells (* p-value<0.05 by unpaired *t* test). **e**, Onset of beating (** p-value<0.01, *** p-value<0.001 by unpaired *t* test). **f-j**, Myofibrillar arrangement of cardiomyocytes (* p-value<0.05, **** p-value<0.0001 by Fisher's exact test). **k**,

bioRxiv preprint doi: https://doi.org/10.1101/835603; this version posted November 10, 2019. The copyright holder for this preprint (which was not certified by peer review) is the author/funder, who has granted bioRxiv a license to display the preprint in perpetuity. It is made available under aCC-BY-ND 4.0 International license.

Action potentials by patch clamp of single beating cells for each *TBX5* genotype. **l,** Action potential duration at 90% (APD_{90}) (* FDR<0.05). **m-n**, Traces of calcium transients from single beating cells were analyzed, including time at 90% decay (t_{90} down) (* FDR<0.05, ** FDR<0.01). Error bars represent standard deviation (**d, e**) or standard error (**l, n**) of the mean.

bioRxiv preprint doi: https://doi.org/10.1101/835603; this version posted November 10, 2019. The copyright holder for this preprint (which was not certified by peer review) is the author/funder, who has granted bioRxiv a license to display the preprint in perpetuity. It is made available under aCC-BY-ND 4.0 International license.

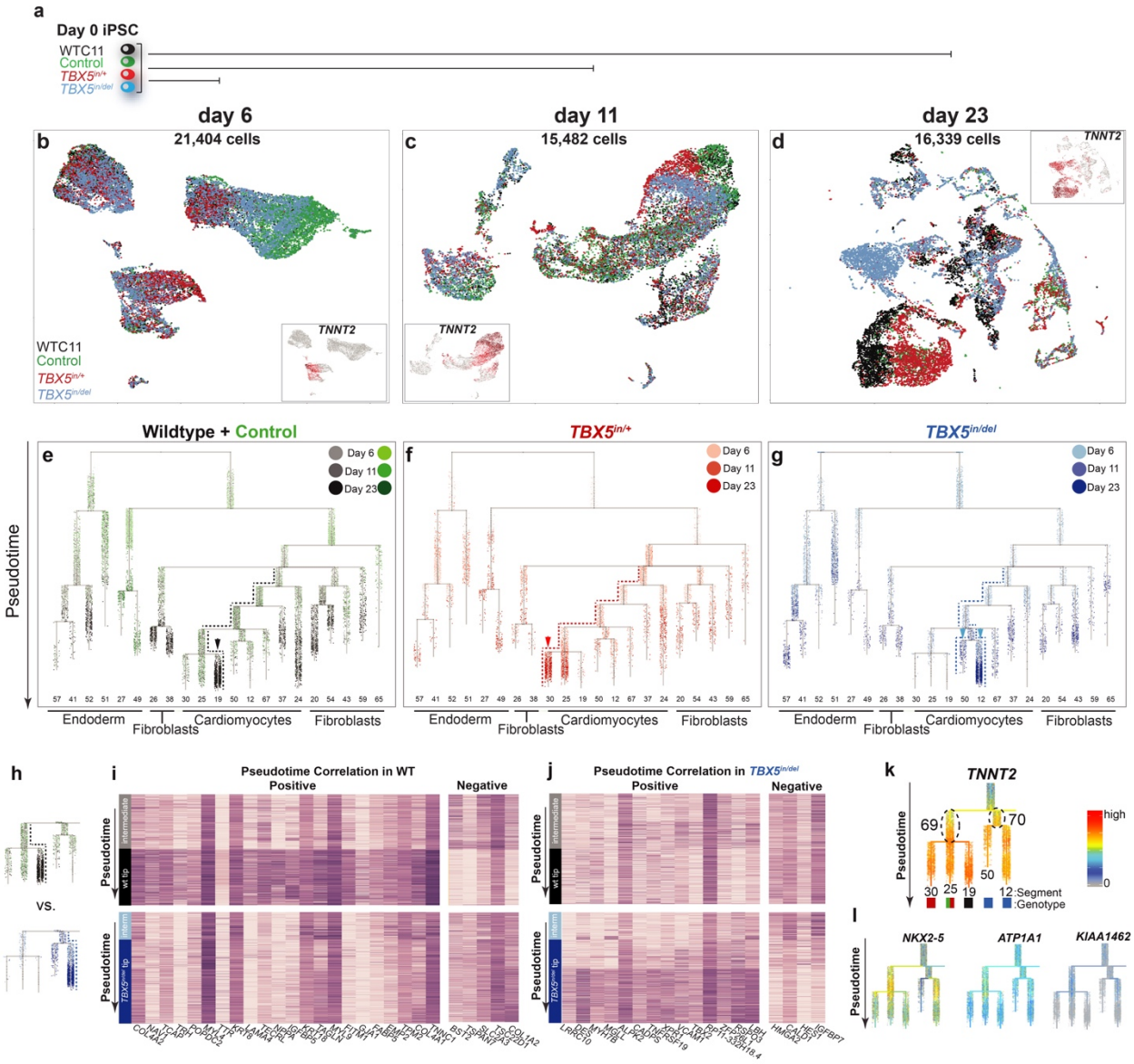

Figure 2. *TBX5* loss disturbs cell trajectories to cardiomyocyte fate. **a**, Cells of each *TBX5* genotype were harvested at specific stages during directed differentiation to cardiomyocytes (CM) for single cell RNAseq. **b-d,** UMAPs display cells at day 6, day 11 or day 23, colored by *TBX5* genotype. A feature plot of the expression of the CM structural gene, *TNNT2*, is shown in each inset. **e-g**, Reconstructed cell trajectories by the R package URD are shown as a dendrogram for each *TBX5* genotype from day 6, 11 and 23, from root (top; early pseudotime) to tips (bottom; late pseudotime). Each *TBX5* genotype is color-coded from light to dark, to indicate time point. Note the enrichment or depletion of cells from one genotype at certain branch points (arrowheads). Dashed lines show inferred path to CMs by *TBX5* genotype. **h**, Deduced paths to non-dividing CMs of WT (black dashed line) or *TBX5*$^{in/del}$ (blue dashed line) are shown, from intermediate (labeled interm) to tip. **i**, Heat maps show expression for each gene that displays a positive or negative correlation with pseudotime (|rho|≥0.4 and Z-score≥15 by difference in rho) in the WT path (above) and is altered in the *TBX5*$^{in/del}$ path (below). **j**, Heat maps show expression for each gene that displays a positive or negative correlation with pseudotime (|rho|≥0.4 and Z-score≥15) in the *TBX5*$^{in/del}$ path and is altered in the WT path

bioRxiv preprint doi: https://doi.org/10.1101/835603; this version posted November 10, 2019. The copyright holder for this preprint (which was not certified by peer review) is the author/funder, who has granted bioRxiv a license to display the preprint in perpetuity. It is made available under aCC-BY-ND 4.0 International license.

(below). **k**, Differential gene expression of inferred precursors for the cardiomyocyte branches (segments 69 vs. 70, dashed ovals) show several genes that display altered gene expression (adj p-value<0.05 by Wilcoxon Rank Sum test) along the WT or *TBX5*$^{in/del}$ path. Colored blocks below represent the predominant *TBX5* genotypes in each tip. **l,** Feature plots show a delayed onset of expression during pseudotime for *NKX2-5,* in addition to *ATP1A1* and *KIAA1462*.

bioRxiv preprint doi: https://doi.org/10.1101/835603; this version posted November 10, 2019. The copyright holder for this preprint (which was not certified by peer review) is the author/funder, who has granted bioRxiv a license to display the preprint in perpetuity. It is made available under aCC-BY-ND 4.0 International license.

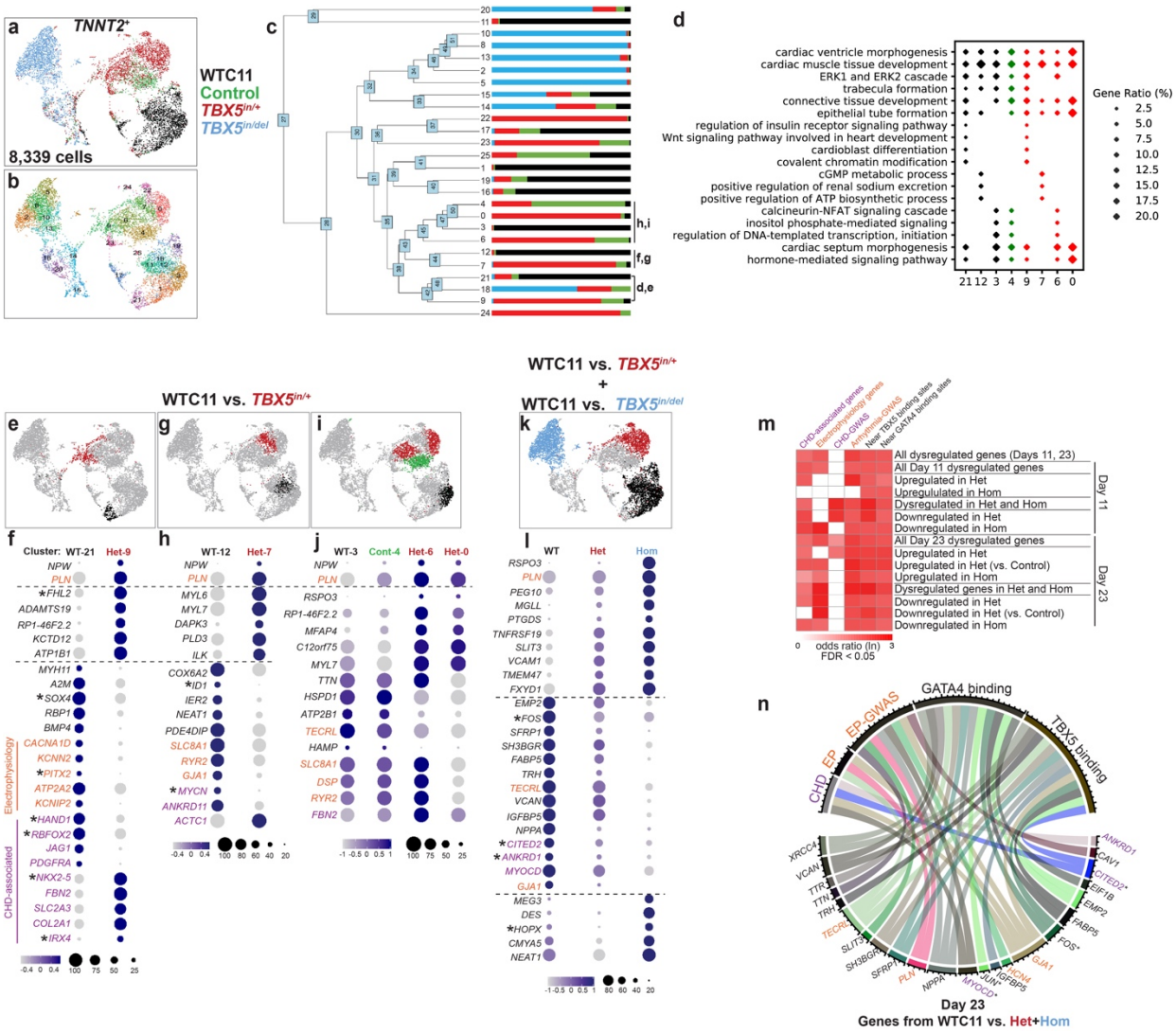

Figure 3. Subsets of cardiomyocytes respond discretely by quantitative transcriptional perturbations to reduced TBX5 dosage. **a-c,** *TNNT2*$^{+}$ clusters from day 23 were re-clustered in Seurat. UMAP shows cells colored by *TBX5* genotype (**a**) or by cluster identity (**b**). **c**, Phylogenetic tree shows the relatedness of the 'average' cell per cluster among clusters. The proportion of cells in each cluster are colored by *TBX5* genotype. Pairs of related clusters between *TBX5* genotypes were selected for differential gene tests. **d,** Gene ontology for enriched biological processes (p-value<0.05 and q-value <0.05) in cell clusters, which are selected for differential gene expression (logfc>0.25 and adj p-value<0.05 by Wilcoxon Rank Sum test), are shown. **e, g, i**, UMAPs highlight clusters used for pair-wise comparisons for differential gene tests in corresponding dot plots below. **f, h**, Dot plots of top differentially expressed genes between wildtype-enriched cluster 21 and *TBX5*$^{in/+}$-enriched cluster 9 (**f**), or between wildtype-enriched cluster 12 and *TBX5*$^{in/+}$-enriched cluster 7 (**h**) (Supplementary Table 2). Each dot size corresponds to the percentage of cells expressing the gene in the cluster, and the color intensity represents scaled expression values in the cluster. Electrophysiology (EP)-related (orange) and congenital heart disease (CHD)-associated (purple) genes are highlighted. Asterisks denote transcription factors. Significance was determined by Wilcoxon Rank Sum test (adj p-value<0.05). **j**, The most differentially expressed genes in *TBX5*$^{in/+}$-enriched clusters 0 and 6, when compared to both wildtype (WT)-enriched cluster 3 or control-enriched cluster 4,

bioRxiv preprint doi: https://doi.org/10.1101/835603; this version posted November 10, 2019. The copyright holder for this preprint (which was not certified by peer review) is the author/funder, who has granted bioRxiv a license to display the preprint in perpetuity. It is made available under aCC-BY-ND 4.0 International license.

are shown. **k**, **l,** UMAP highlights clusters for comparison (**k**) in dot plots of genes that are most differentially expressed in both *TBX5*$^{in/+}$- and *TBX5*$^{in/del}$-enriched clusters, when compared to WT-enriched clusters (**l**). **m**, Heat map displays significant correlations (adj p-value<0.05 by Benjamini-Hochberg multiple corrections test) among comparisons of candidate lists for CHD-associated genes, EP-related genes, genome-wide association studies (GWAS) for CHDs or arrhythmias (Supplementary Table 4), and TBX5-dependent gene sets. **n**, Circular plot shows selected genes by category for WT-enriched vs. *TBX5*$^{in/+}$-enriched and WT-enriched vs. *TBX5*$^{in/del}$-enriched clusters at day 23.

bioRxiv preprint doi: https://doi.org/10.1101/835603; this version posted November 10, 2019. The copyright holder for this preprint (which was not certified by peer review) is the author/funder, who has granted bioRxiv a license to display the preprint in perpetuity. It is made available under aCC-BY-ND 4.0 International license.

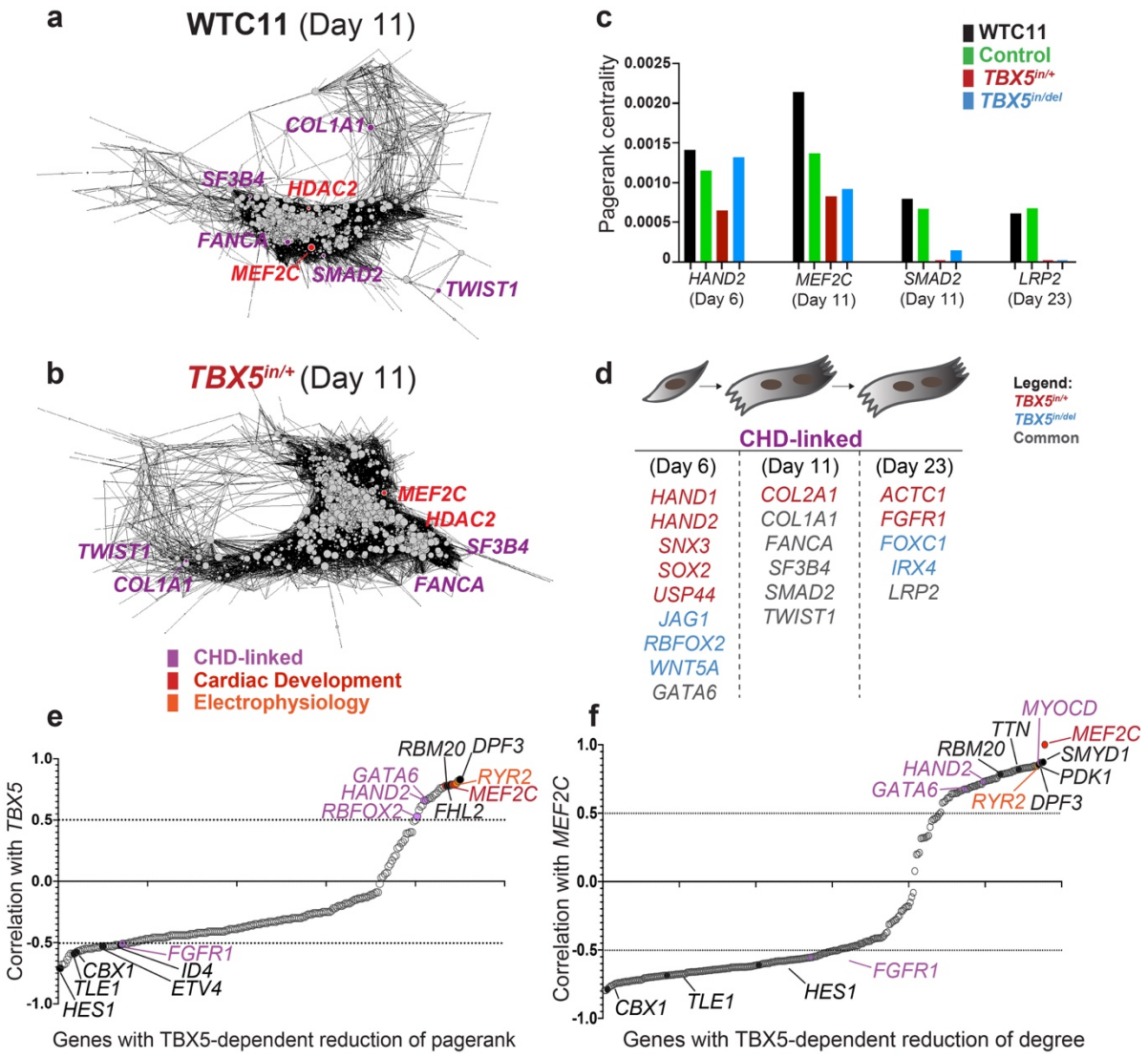

Figure 4. TBX5 dosage preserves cardiomyocyte network stability. a, b, Gene regulatory networks (GRNs) for day 11 cardiomyocytes of WTC11 (**a**) or *TBX5*$^{in/+}$ (**b**) are shown. Nodes of CHD-related (purple), heart development (red) or electrophysiology (orange) genes are shown. The size of each node represents its quantitative importance, based on pagerank centrality. Note the absence of *SMAD2* and the reduced centrality of *MEF2C* (smaller circle) in the *TBX5*$^{in/+}$ network, compared to WTC11. **c**, Pagerank centrality for significantly altered (top 5% cutoff) nodes of CHD-associated or heart development genes at specific time points are shown. **d,** Twenty CHD-associated genes display a reduction in pagerank (top 5% cutoff) in at least one mutant *TBX5* genotype at any stage. This indicates enrichment of CHD-associated genes in TBX5 dosage-sensitive networks (p<2.2e-5 by hypergeometric test). **e,** TBX5-dependent genes with a reduction of pagerank are correlated (correlation >0.5), anti-correlated (correlation <-0.5), or indeterminate (0.5<correlation<-0.5) with *TBX5* expression in *TNNT2*$^{+}$ cells. **f,** Correlations with *MEF2C* and TBX5-dependent genes with a reduction of degree in *TNNT2*$^{+}$ cells are plotted. Additional data can be found in Supplementary Table 3.

bioRxiv preprint doi: https://doi.org/10.1101/835603; this version posted November 10, 2019. The copyright holder for this preprint (which was not certified by peer review) is the author/funder, who has granted bioRxiv a license to display the preprint in perpetuity. It is made available under aCC-BY-ND 4.0 International license.

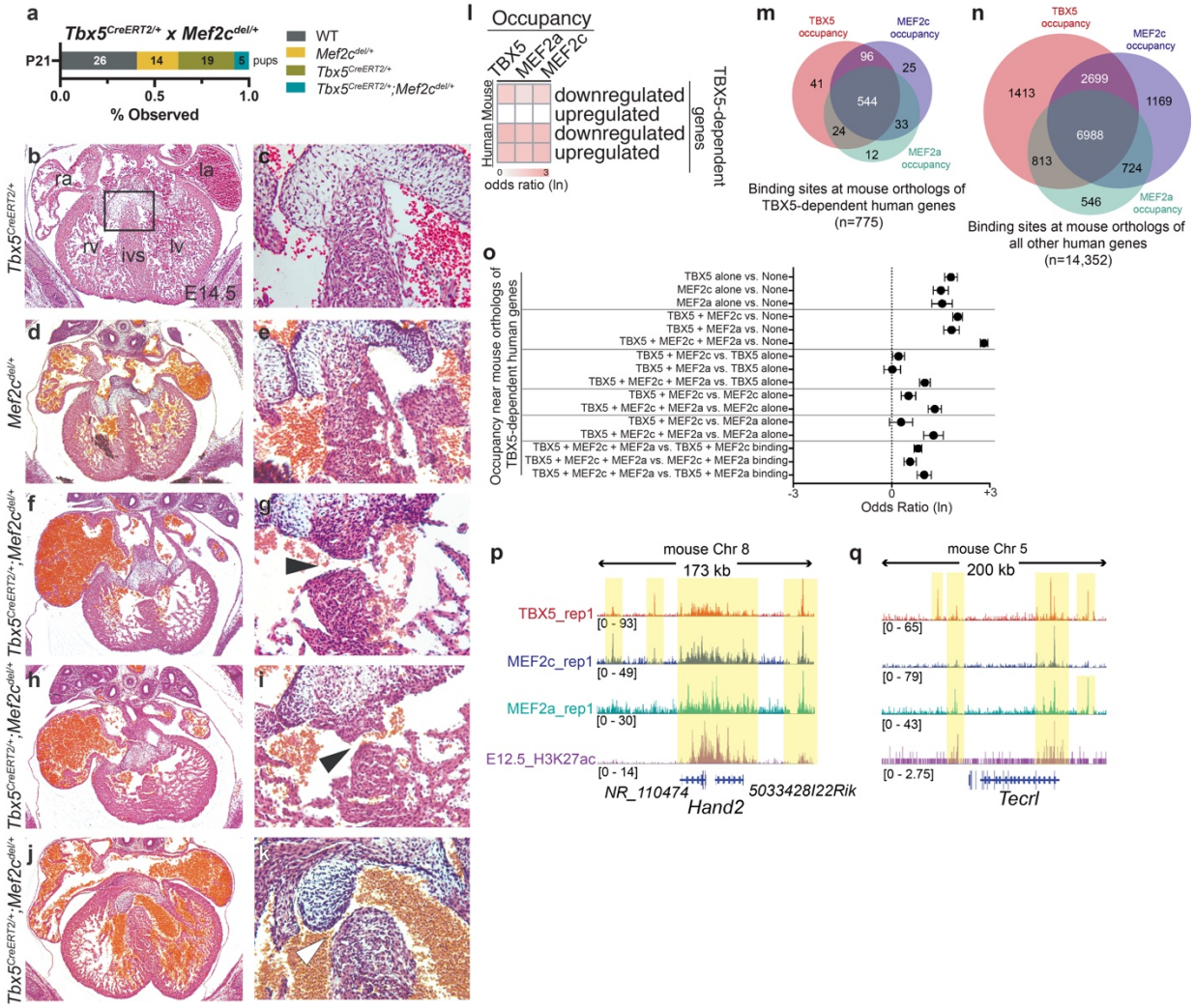

Figure 5. *Tbx5* and *Mef2c* cooperate in heart development. a, Pups at post-natal day 21 (P21) from matings of *Tbx5*$^{CreERT2/+}$ X *Mef2c*$^{del/+}$ were genotyped. Expected Mendelian ratios were not observed for *Tbx5*$^{CreERT2/+}$;*Mef2c*$^{del/+}$ at P21. **b, d, f, h, j**, Transverse sections of hearts at embryonic day 14.5 (E14.5) from each genotype are shown. **c, e, g, i, k**. Magnified views of the interventricular septa are shown. Note muscular VSDs (black arrowheads in **g, i**), a subaortic membranous VSD (**k**, white arrowhead) and dilated blood-filled atria in the *Mef2c*$^{+/-}$;*Tbx5*$^{CreERT2/+}$ embryos (**f, h, j**). **l,** Heat map indicates odds ratios (FDR<0.05) of TBX5, MEF2a or MEF2c occupancy near mouse or human TBX5-dependent genes (Supplementary Table 6). **m, n,** Venn diagrams display the overlap of TBX5, MEF2a or MEF2c occupancy near mouse orthologs of human TBX5-dependent or -independent genes, respectively. **o,** Odds ratio (FDR<0.05) of combinations of TBX5, MEF2a or MEF2c occupancy near mouse orthologs of TBX5-dependent human genes (Supplementary Table 6). **p, q,** Browser tracks for ChIP-seq data from E12.5 hearts for TBX5, MEF2c, MEF2a and H3K27ac near conserved TBX5-dependent genes, *Hand2* (**p**) or *Tecrl* (**q**). Yellow bands of shading indicate co-occupancy.

bioRxiv preprint doi: https://doi.org/10.1101/835603; this version posted November 10, 2019. The copyright holder for this preprint (which was not certified by peer review) is the author/funder, who has granted bioRxiv a license to display the preprint in perpetuity. It is made available under aCC-BY-ND 4.0 International license.

a

		Genotype	Translation
	WTC11	+/+	
+ Cas9	Control	+/+	
+ Cas9	*TBX5*$^{in/+}$	ins 2bp/+	p.M51fs*16/+
+ Cas9	*TBX5*$^{in/del}$	ins 1bp / del 8bp	p.M51fs*10/p.M51fs*7
+ Cas9	*TBX5*$^{PuR/PuR}$	ins PGK-PuroR/ins PGK-PuroR	

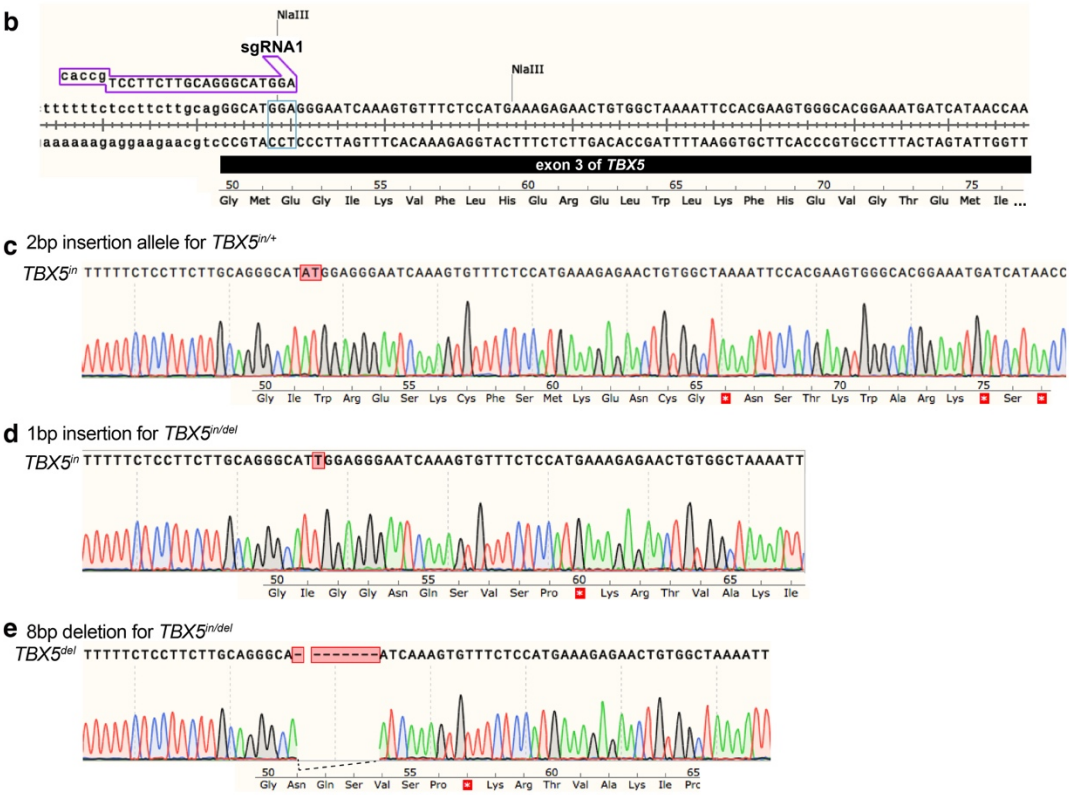

984

986 **Extended Data 1. Genotype information for targeted WTC11-derived iPS cells mutant for *TBX5*. a,** Table shows genotypes of WTC11-derived iPS cell lines that were targeted for *TBX5*
988 at exon 3. Predicted translation for each *TBX5* genotype is indicated. **b**, Sequence of the exon 3 of *TBX5* is shown, along with the sgRNA1 location. The PAM site is boxed in blue. Loss of the
990 NlaIII site at the PAM site was used in initial screening for mutant iPS cell clones by PCR. The encoded wildtype protein sequence includes the start of the T-box domain. **c**, Sequence and
992 chromatogram for the 2bp insertion of the mutant allele for *TBX5*$^{in/+}$ predicts a premature truncation, as indicated by a stop codon (white asterisk in red box) in the frame-shifted protein
994 sequence. **d**, **e**, Sequence and chromatogram for the 1 bp insertion, or 8 bp deletion, respectively, of the mutant allele for *TBX5*$^{in/del}$, along with corresponding protein sequences, are
996 shown.

bioRxiv preprint doi: https://doi.org/10.1101/835603; this version posted November 10, 2019. The copyright holder for this preprint (which was not certified by peer review) is the author/funder, who has granted bioRxiv a license to display the preprint in perpetuity. It is made available under aCC-BY-ND 4.0 International license.

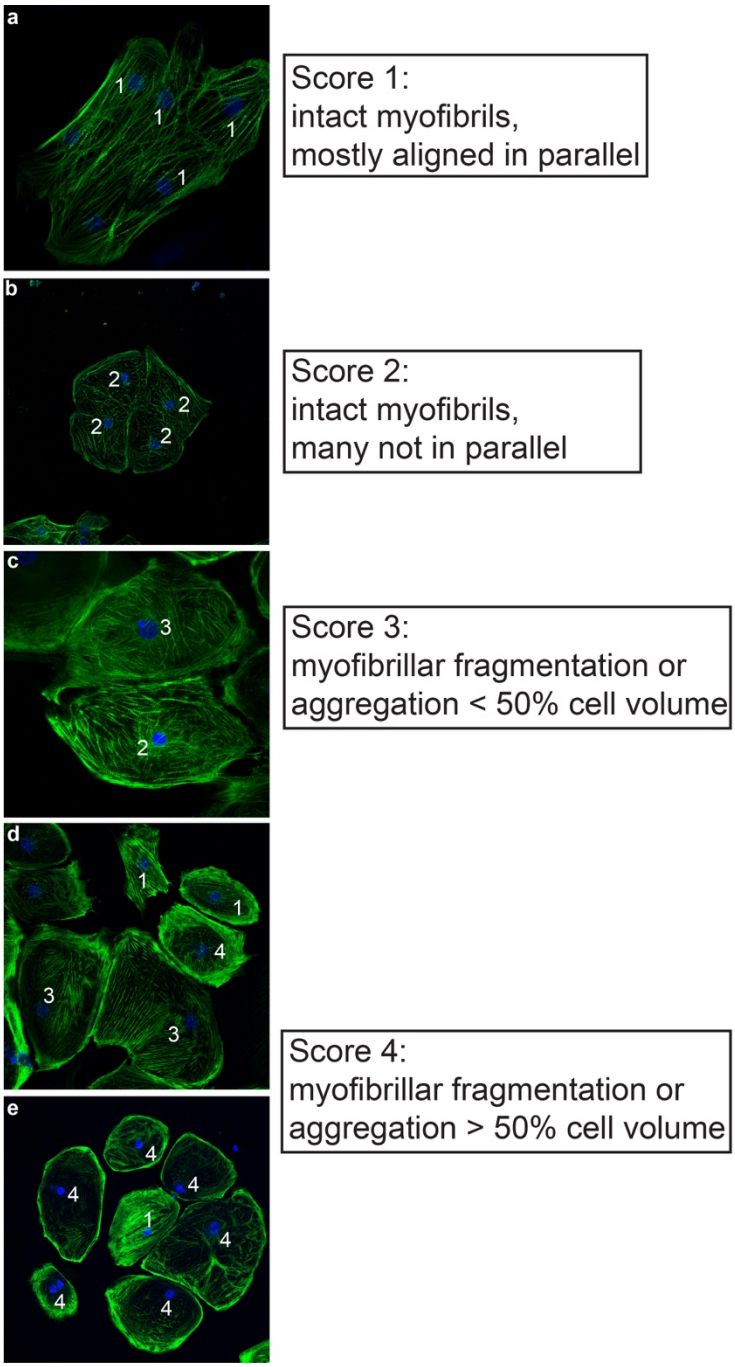

Extended Data 2. Scoring criteria for myofibrillary disarray. Criteria for scores 1-5 are indicated, and representative images for each score are shown.

bioRxiv preprint doi: https://doi.org/10.1101/835603; this version posted November 10, 2019. The copyright holder for this preprint (which was not certified by peer review) is the author/funder, who has granted bioRxiv a license to display the preprint in perpetuity. It is made available under aCC-BY-ND 4.0 International license.

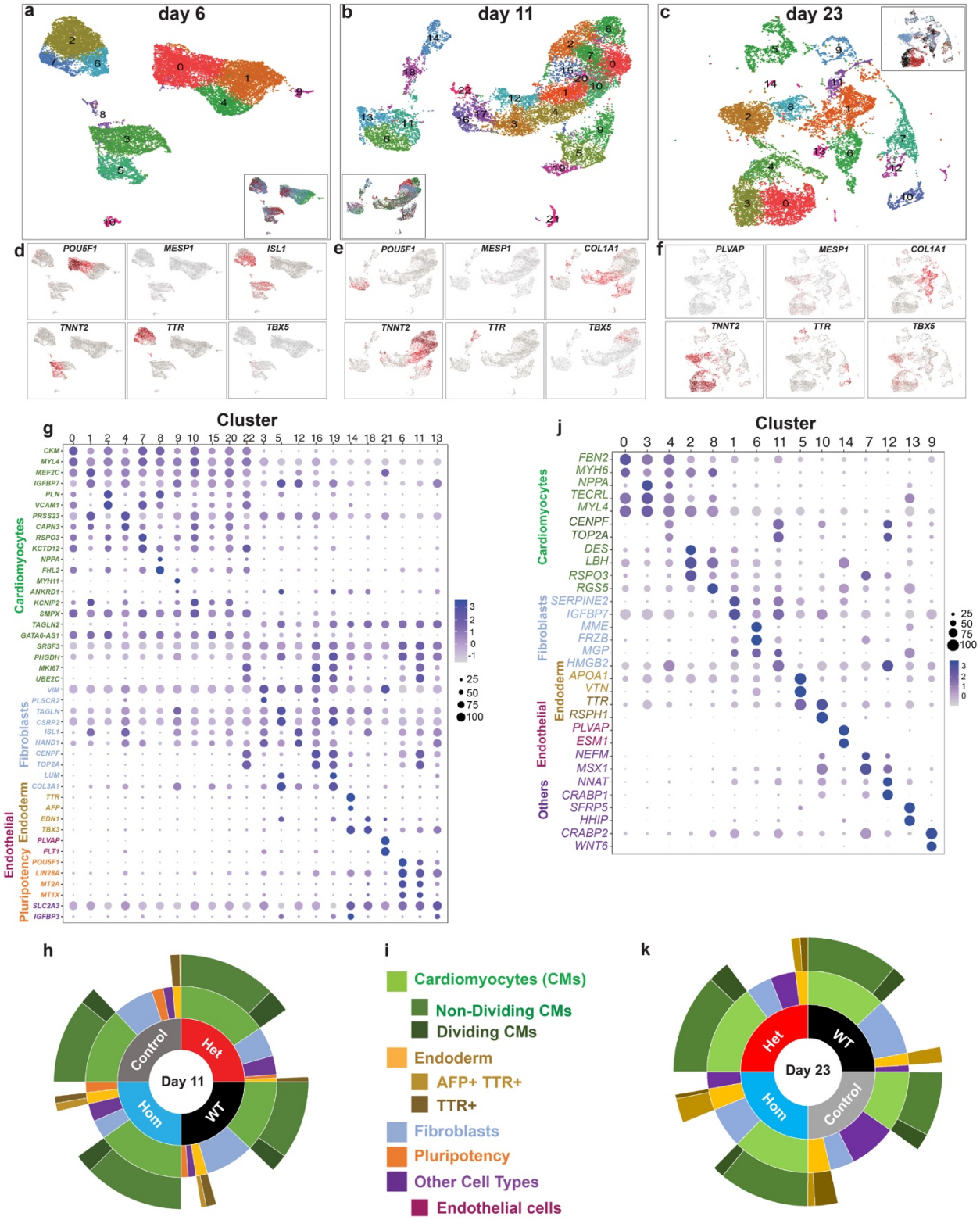

bioRxiv preprint doi: https://doi.org/10.1101/835603; this version posted November 10, 2019. The copyright holder for this preprint (which was not certified by peer review) is the author/funder, who has granted bioRxiv a license to display the preprint in perpetuity. It is made available under aCC-BY-ND 4.0 International license.

Extended Data 3. Human cardiac differentiation is sensitive to reduced TBX5 dosage. a-c, UMAPs display cells at day 6, day 11 and day 23, respectively, by Louvain clustering. Insets show UMAPs colored by *TBX5* genotype. **d-f**, Feature plots in UMAP space demonstrate expression of selected marker genes, which represent major cell types at each timepoint. **g, j**, Dot plots display two of the top marker genes that are expressed in each cluster at day 11 or day 23 (adj p-value<0.05 by Wilcoxon Rank Sum test), and define at least five major human cell types. The size of the dot corresponds to the percentage of cells expressing the gene in the cluster, and the color intensity represents the level of gene expression in the cluster. **h, i, k**, Sunburst plots indicate the proportion of at least five major cell types, based on top marker genes, by *TBX5* genotype at day 11 or day 23.

bioRxiv preprint doi: https://doi.org/10.1101/835603; this version posted November 10, 2019. The copyright holder for this preprint (which was not certified by peer review) is the author/funder, who has granted bioRxiv a license to display the preprint in perpetuity. It is made available under aCC-BY-ND 4.0 International license.

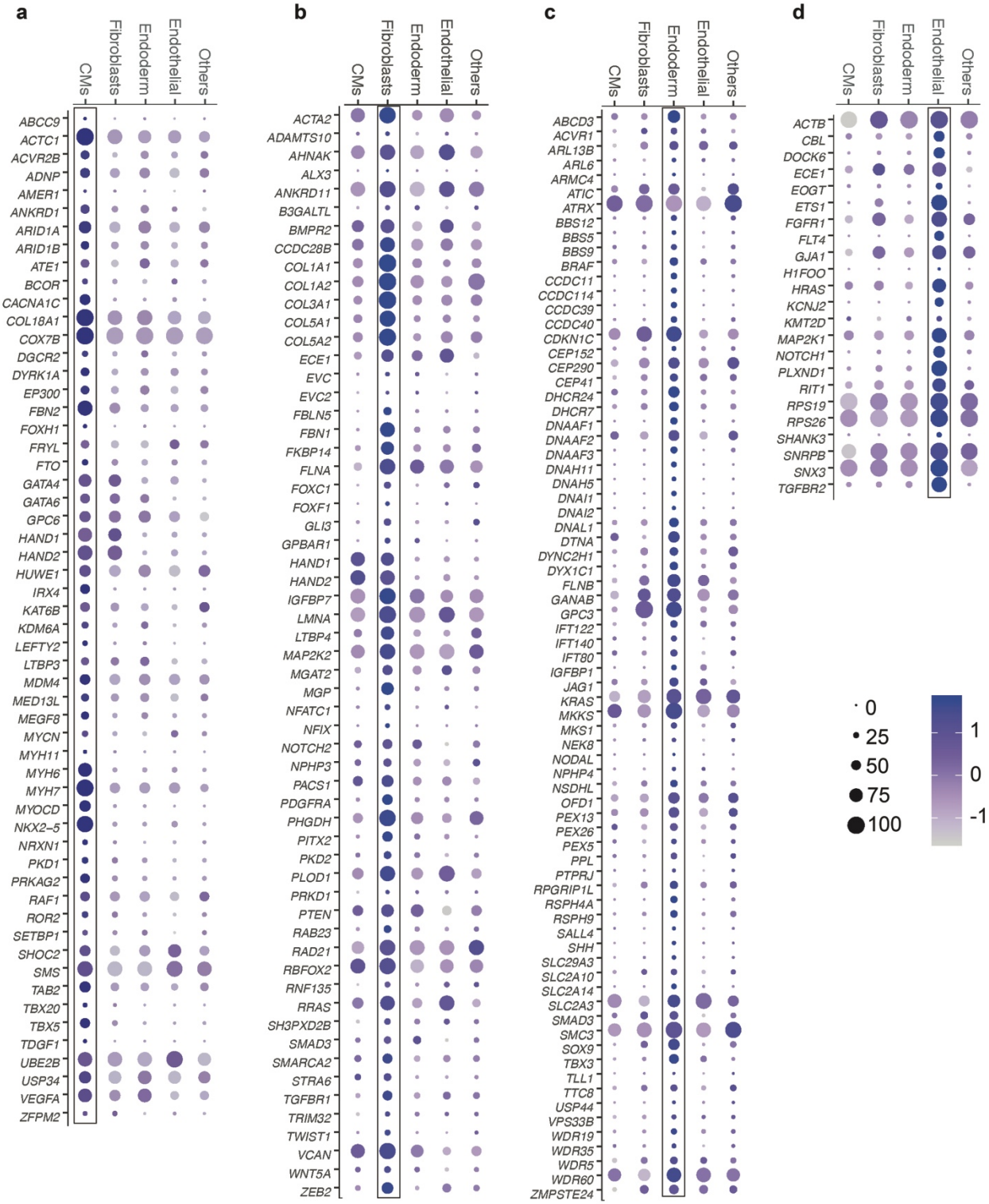

Extended Data 4. Many CHD-associated genes are enriched among several human cell types. a-d, Dot plots show the expression of congenital heart disease (CHD)-associated genes that are significantly enriched in cardiomyocytes (**a**), fibroblasts (**b**), endodermal cells (**c**) or

bioRxiv preprint doi: https://doi.org/10.1101/835603; this version posted November 10, 2019. The copyright holder for this preprint (which was not certified by peer review) is the author/funder, who has granted bioRxiv a license to display the preprint in perpetuity. It is made available under aCC-BY-ND 4.0 International license.

endothelial cells (**d**). Significance was determined by Wilcoxon Rank Sum test (adj p-value<0.05).

bioRxiv preprint doi: https://doi.org/10.1101/835603; this version posted November 10, 2019. The copyright holder for this preprint (which was not certified by peer review) is the author/funder, who has granted bioRxiv a license to display the preprint in perpetuity. It is made available under aCC-BY-ND 4.0 International license.

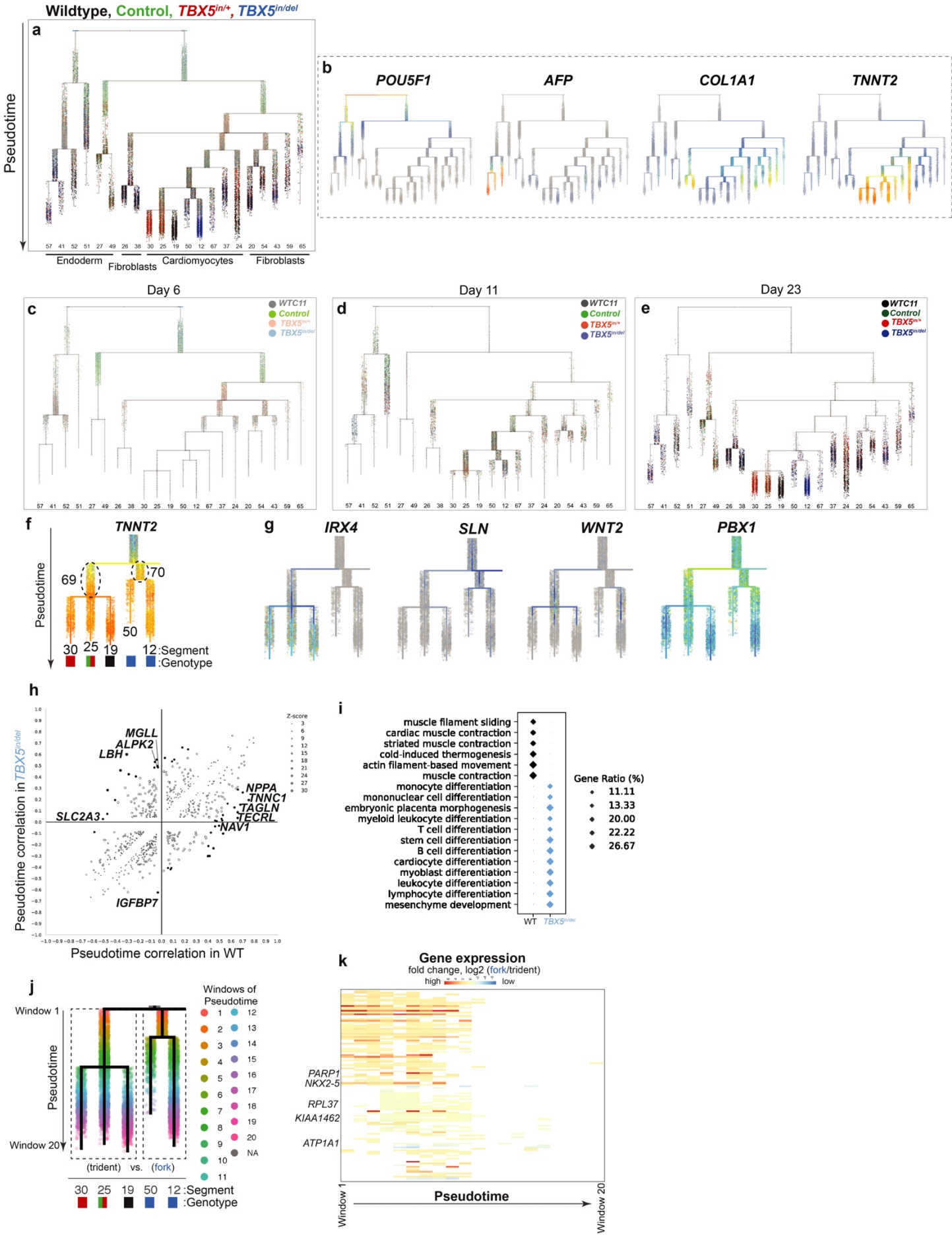

bioRxiv preprint doi: https://doi.org/10.1101/835603; this version posted November 10, 2019. The copyright holder for this preprint (which was not certified by peer review) is the author/funder, who has granted bioRxiv a license to display the preprint in perpetuity. It is made available under aCC-BY-ND 4.0 International license.

Extended Data 5. Pseudotime analysis of cell trajectory reconstructions by genotype, time point and cell type. a, All cells for all *TBX5* genotypes and time points are shown for directed differentiation to cardiomyocytes in a single plot. Pseudotime is displayed from root (top) to tips (bottom). **b,** Genes, which mark each major cell type (pluripotent cell, endoderm, fibroblast and cardiomyocyte) during the directed differentiation, are shown. **c-e**, Cells from all *TBX5* genotypes are shown by time point. **f,** Differential gene expression between inferred precursors (dashed ovals, segments 69 vs. 70) of the WT or *TBX5*$^{in/del}$ path was evaluated. **g**, Delayed activation of *WNT2*, *PBX1* and *NKX2-5* in the *TBX5*$^{in/del}$ path (to segments 50 and 12) diverged from the path of other genotypes (to segments 20, 25, 19). *IRX4* was absent in the *TBX5*$^{in/del}$ path, and instead, *SLN* was enriched. Significance was determined by Wilcoxon Rank Sum test (adj p-value<0.05). **h**, Scatter plot displays two axes of Spearman rho correlations, which measure a potential relationship between gene expression and pseudotime for WT or *TBX5*$^{in/del}$ cell. Each white circle represents a gene that has a significant rho correlation with pseudotime (p-value<0.05 by two-sided *t* test). Size of the circle represents a Z-score difference for rho correlation of a gene to pseudotime for WT versus *TBX5*$^{in/del}$ path. As the size of the circle increases, there is a larger difference in how a gene is correlated with pseudotime between the two genotypes. Black circles represent genes with a moderate correlation or better with pseudotime in either path (|rho|≥0.4) and (Z-score≥15), when the opposing genotype has no significant correlation to pseudotime (p-value≥0.05 by two-sided *t* test). **i**, Gene ontology (GO) terms for enriched biological processes (p-value<0.05 and q-value<0.05), which are based on genes that positively correlate with pseudotime (|rho|≥0.4 and Z-score≥15 by difference in rho) in the WT- or the *TBX5*$^{in/del}$ path, are shown. Black (WT) or blue (*TBX5*$^{in/del}$) diamonds show gene ratios. **j,** Deduced paths for WT/control/ *TBX5*$^{in/+}$(trident) or *TBX5*$^{in/del}$ (fork) to cardiomyocytes were divided into windows (1-20) along pseudotime for comparison. **k**, Heat map shows fold change for genes in a cluster that includes *NKX2-5,* which was significantly different after correction (adj p-value<0.05 by Bonferroni-Holm test) in windows 2 through 8, along with genes of a similar pattern, including *PARP1, RPL37, KIAA1462,* and *ATP1A1* (adj p-value<0.05 by Bonferroni-Holm test).

bioRxiv preprint doi: https://doi.org/10.1101/835603; this version posted November 10, 2019. The copyright holder for this preprint (which was not certified by peer review) is the author/funder, who has granted bioRxiv a license to display the preprint in perpetuity. It is made available under aCC-BY-ND 4.0 International license.

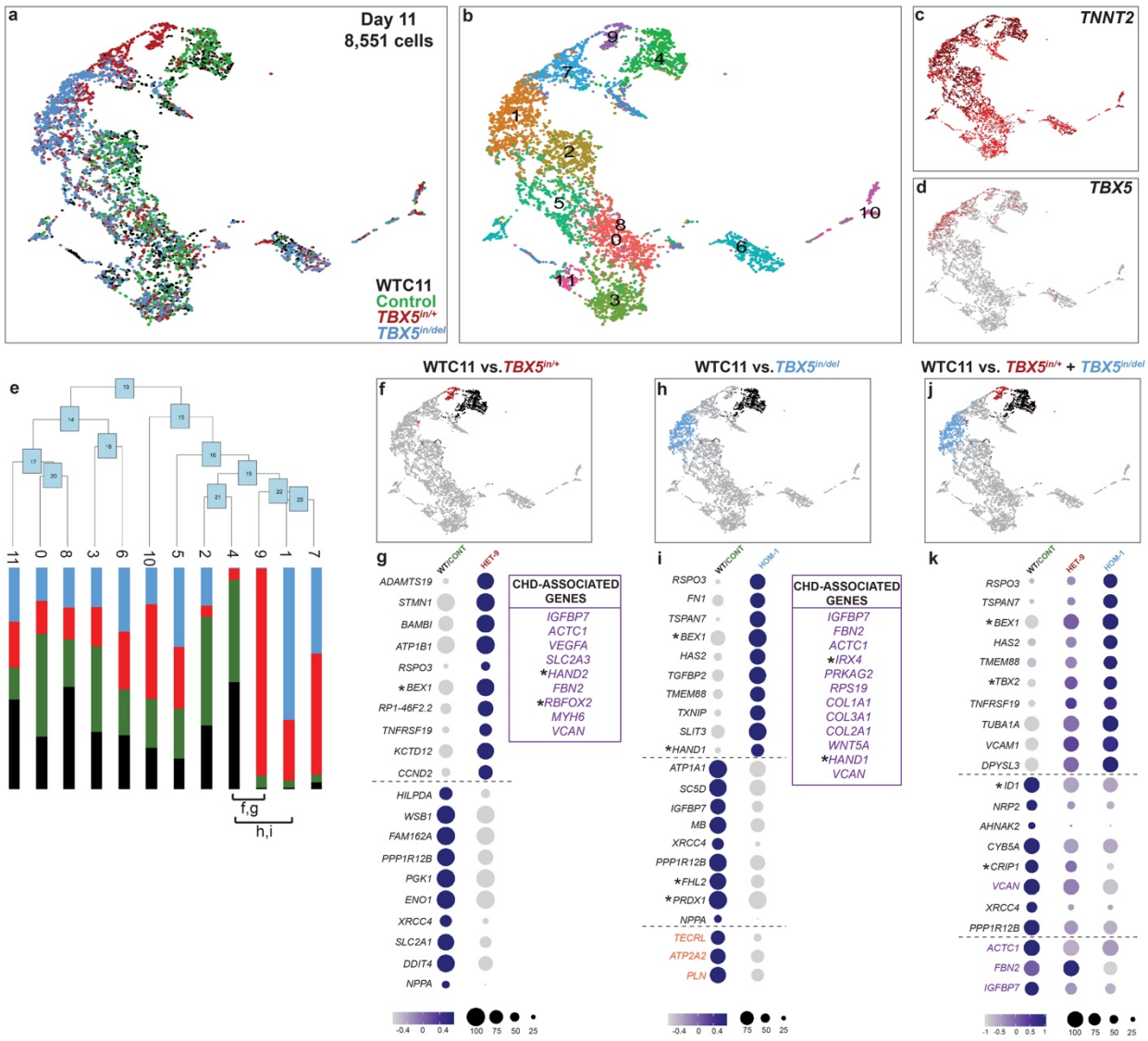

Extended Data 6. Evaluation of reduced TBX5 dosage by gene expression in cardiomyocytes at day 11. **a, b**, UMAPs of *TNNT2*$^{+}$ cells from day 11 of differentiation are colored by *TBX5* genotype or by cluster identity, respectively. **c, d**, Feature plots by UMAP display expression of *TNNT2* or *TBX5*. **e,** Phylogenetic tree depicts cluster relatedness. Vertical bars show the proportion of cells by color of each *TBX5* genotype. **f, h,** UMAPs highlight clusters chosen for pair-wise differential gene expression comparisons. **g, i**, Dot plots show top differentially expressed genes between WT/control-enriched and *TBX5*$^{in/+}$-enriched clusters, or WT/control-enriched and *TBX5*$^{in/del}$-enriched clusters, respectively. Electrophysiology-related (orange) and congenital heart disease (CHD)-associated (purple) genes are highlighted. Significance was determined by Wilcoxon Rank Sum test (adj p-value<0.05). **j**, UMAP demonstrates pair-wise comparisons between WT/control-enriched and *TBX5*$^{in/+}$-enriched clusters, and WT/control-enriched and *TBX5*$^{in/+}$-enriched clusters. **k**, Common genes that are differentially expressed in both *TBX5*$^{in/+}$ and *TBX5*$^{in/del}$, in each comparison with WT/control are shown.

bioRxiv preprint doi: https://doi.org/10.1101/835603; this version posted November 10, 2019. The copyright holder for this preprint (which was not certified by peer review) is the author/funder, who has granted bioRxiv a license to display the preprint in perpetuity. It is made available under aCC-BY-ND 4.0 International license.

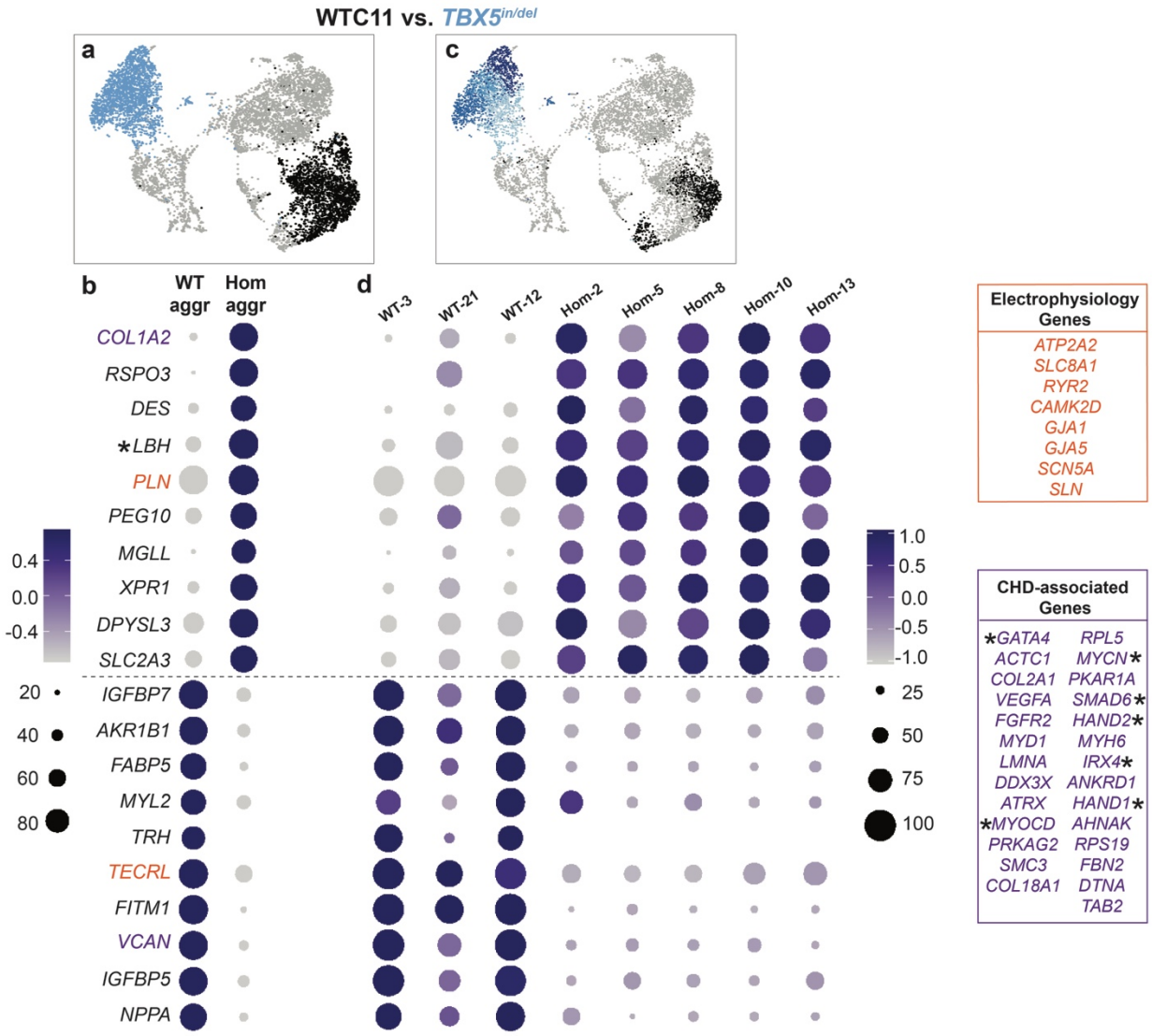

Extended Data 7. Loss of *TBX5* by gene expression in individual cardiomyocytes at day 23. a, UMAP of day 23 cardiomyocytes displays a wildtype-enriched (black) and *TBX5*$^{in/del}$-enriched (blue) cluster, at a low Louvain resolution in Seurat, for comparison between clusters of *TBX5* genotypes. **b**, Dot plots showing top differentially expressed genes between aggregate WT-enriched and *TBX5*$^{in/del}$-enriched clusters. Transcriptional regulators are denoted by asterisks. Electrophysiology-related (orange) and congenital heart disease (CHD)-associated (purple) are highlighted. Significance was determined by Wilcoxon Rank Sum test (adj p-value<0.05). **c**, UMAP shows clusters at a higher resolution, with three wildtype-enriched (black) sub-clusters and five *TBX5*$^{in/del}$-enriched (shades of blue) sub-clusters. **d,** Heterogeneity of gene expression among labeled sub-clusters are shown.

bioRxiv preprint doi: https://doi.org/10.1101/835603; this version posted November 10, 2019. The copyright holder for this preprint (which was not certified by peer review) is the author/funder, who has granted bioRxiv a license to display the preprint in perpetuity. It is made available under aCC-BY-ND 4.0 International license.

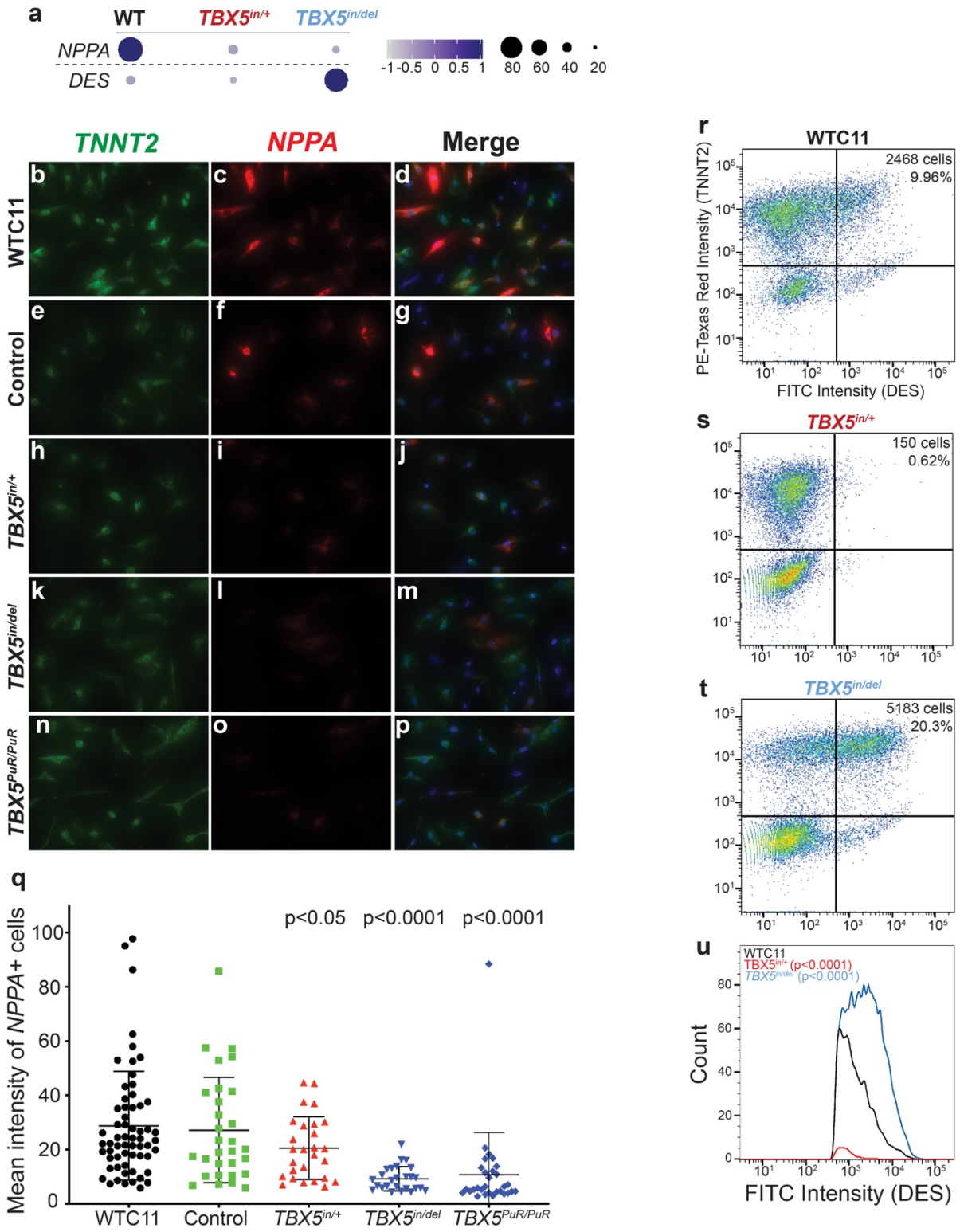

Extended Data 8. Single cell analysis of TBX5-dependent genes by orthogonal assays. a, Dot plots show expression of *NPPA* and *DES* in WTC11 (WT)-, *TBX5*$^{in/+}$- and *TBX5*$^{in/del}$ -enriched clusters at day 23. **b-p,** Fluorescence *in situ* hybridization is visualized for *TNNT2*

bioRxiv preprint doi: https://doi.org/10.1101/835603; this version posted November 10, 2019. The copyright holder for this preprint (which was not certified by peer review) is the author/funder, who has granted bioRxiv a license to display the preprint in perpetuity. It is made available under aCC-BY-ND 4.0 International license.

(green) or *NPPA* (red) in day 23 cardiomyocytes, from (**b-d**) WTC11, (**e-g**) control, (**h-j**) *TBX5*$^{in/+}$, (**k-m**) *TBX5*$^{in/del}$ and (**n-p**) *TBX5*$^{PuR/PuR}$ cells. **q,** Graph displays mean intensity of *NPPA* signal of individual double-positive *TNNT2*$^{+}$/*NPPA*$^{+}$ cells by *TBX5* genotype. Significance of p-values were calculated by unpaired *t* test. **r-t,** Pseudocolor plots showing cTNT^{+} and DES^{+} double positive cells in (**r**) wildtype, (**s**) *TBX5*$^{in/+}$ or (**t**) *TBX5*$^{in/del}$ at day 23. **u,** Histogram of FITC intensity of DES^{+} cells from wildtype, *TBX5*$^{in/+}$ or *TBX5*$^{in/del}$ cells is shown (****p-value<1E-4 by Chi-Square test).

bioRxiv preprint doi: https://doi.org/10.1101/835603; this version posted November 10, 2019. The copyright holder for this preprint (which was not certified by peer review) is the author/funder, who has granted bioRxiv a license to display the preprint in perpetuity. It is made available under aCC-BY-ND 4.0 International license.

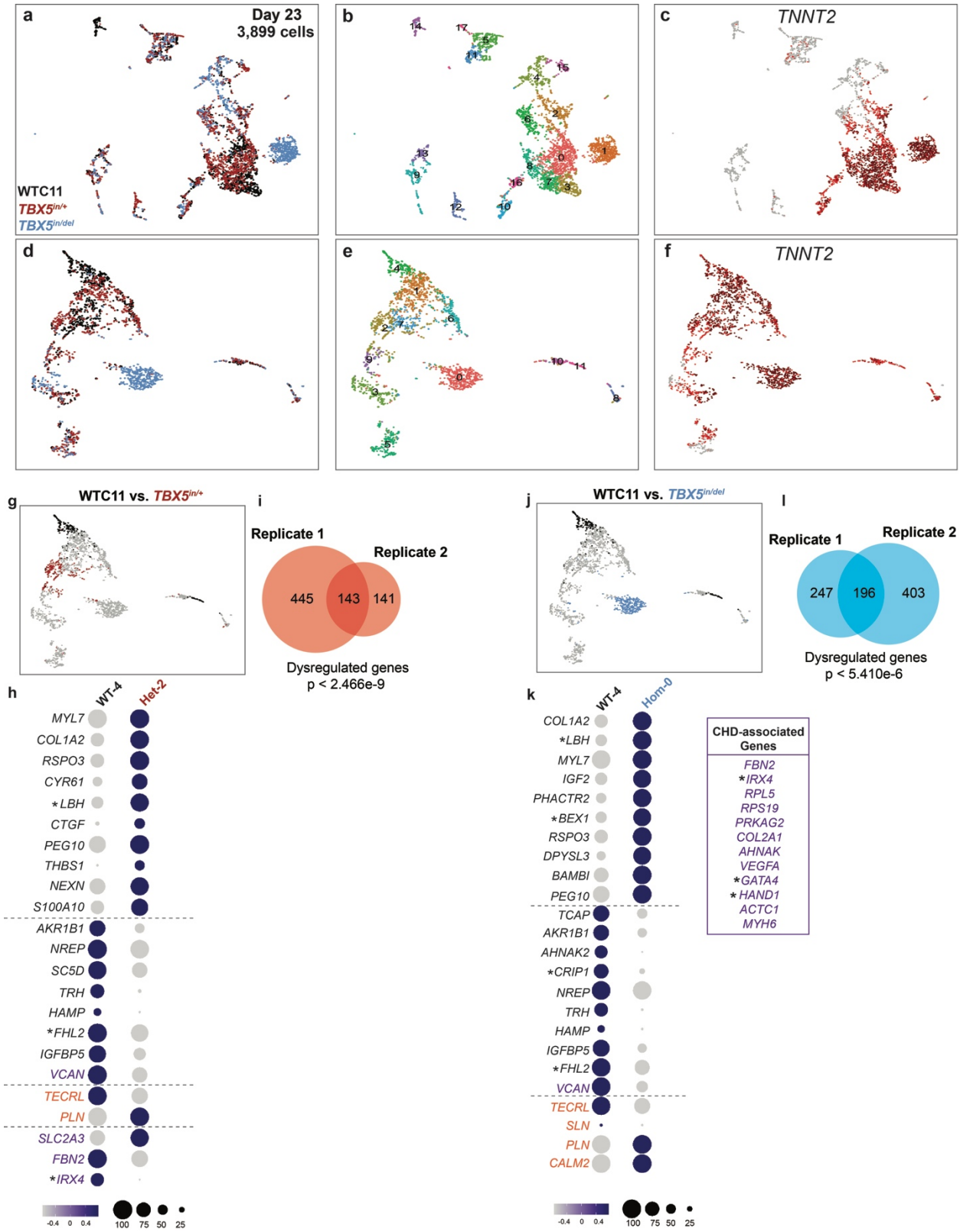

1104

bioRxiv preprint doi: https://doi.org/10.1101/835603; this version posted November 10, 2019. The copyright holder for this preprint (which was not certified by peer review) is the author/funder, who has granted bioRxiv a license to display the preprint in perpetuity. It is made available under aCC-BY-ND 4.0 International license.

Extended Data 9. Biological replicate of TBX5 dose-sensitive responses in WTC11-derived cardiomyocytes at day 23. a, b, Cells at day 23 of an independent differentiation (biological replicate) were collected for single cell RNAseq analysis. UMAP shows all cells from day 23 colored by *TBX5* genotype or by cluster identity, respectively. **c,** UMAP shows *TNNT2* expression. **d, e,** UMAP of *TNNT2*$^{+}$ cells from day 23 are colored by *TBX5* genotype or by cluster identity, respectively. **f,** UMAP shows *TNNT2* expression in *TNNT2*$^{+}$ cells. **g, j,** UMAPs highlight clusters used in pair-wise differential gene tests. **h, k,** Dot plots show top differentially expressed genes between wildtype (WT)-enriched and *TBX5*$^{in/+}$-enriched or *TBX5*$^{in/del}$-enriched clusters (Supplementary Table 2). Electrophysiology-related (orange) or congenital heart disease (CHD)-associated (purple) genes are indicated. Asterisks denote transcription factors. Significance was determined by Wilcoxon Rank Sum test (adj p-value<0.05). **i, l,** Venn diagrams show overlap of differentially expressed genes detected in the first and second biological replicates at day 23. Statistical significance was determined by Hypergeometric test, based on the union of highly variable genes from both datasets (1,688) as the population size.

bioRxiv preprint doi: https://doi.org/10.1101/835603; this version posted November 10, 2019. The copyright holder for this preprint (which was not certified by peer review) is the author/funder, who has granted bioRxiv a license to display the preprint in perpetuity. It is made available under aCC-BY-ND 4.0 International license.

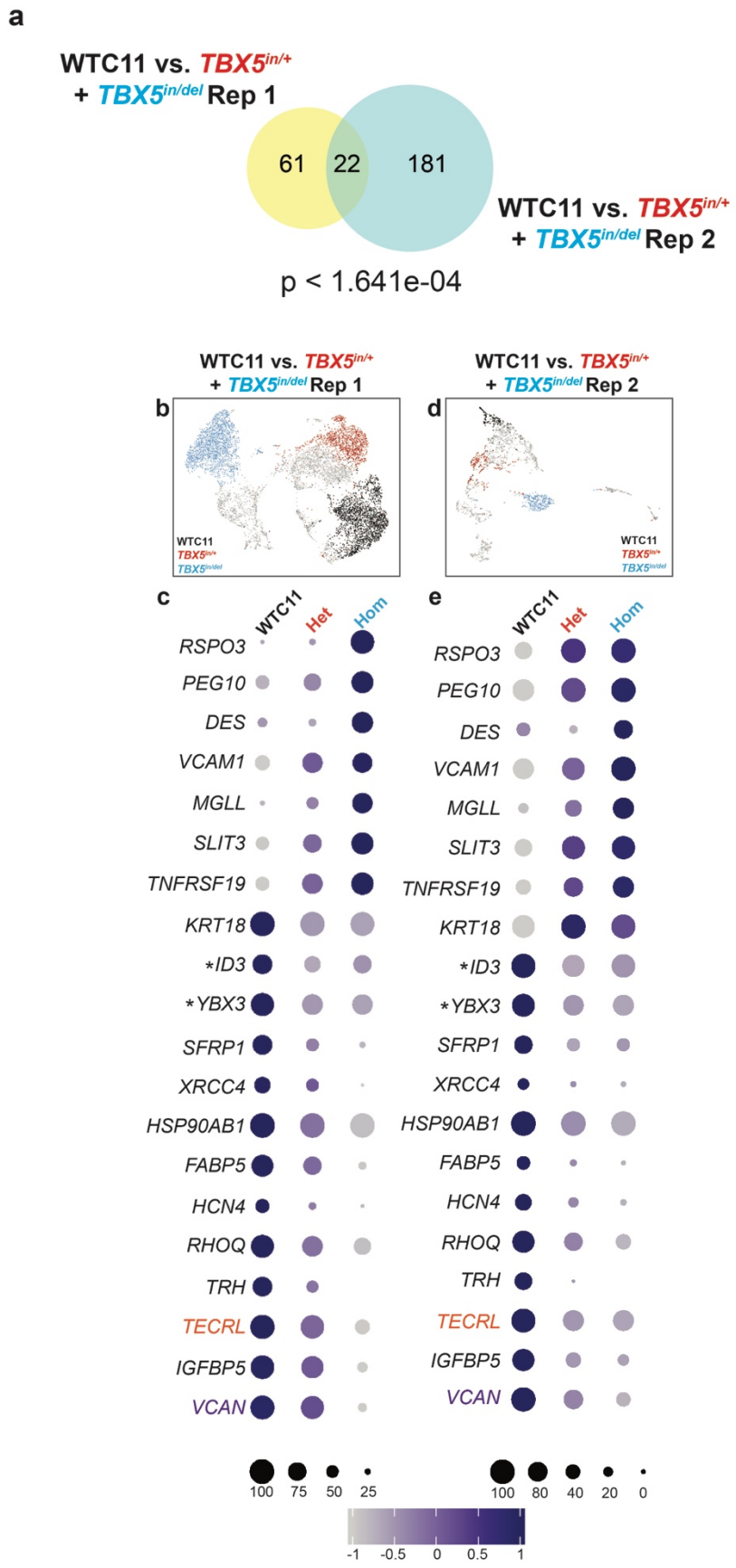

bioRxiv preprint doi: https://doi.org/10.1101/835603; this version posted November 10, 2019. The copyright holder for this preprint (which was not certified by peer review) is the author/funder, who has granted bioRxiv a license to display the preprint in perpetuity. It is made available under aCC-BY-ND 4.0 International license.

Extended Data 10. Overlap of TBX5 dose-dependent genes between biological replicates. **a,** Venn diagram shows overlap of differentially expressed genes detected at day 23 in WTC11-targeted *TBX5*$^{in/+}$ and *TBX5*$^{in/del}$ cells from biological replicate 1 and replicate 2. Statistical significance was determined by Hypergeometric test, based on the union of highly variable genes from both datasets (1,688) as the population size. **b, d,** UMAPs demonstrate clusters chosen for differential gene expression within each experiment for comparison. **c, e,** Dot plots show top differentially expressed genes for replicates. Significance was determined by Wilcoxon Rank Sum test (adj p-value<0.05). **f,** Venn diagram shows overlap of differentially expressed genes between genetic backgrounds of WTC11-targeted *TBX5*$^{in/+}$ and *TBX5*$^{in/del}$ cells and PGP1-targeted *TBX5*$^{in/+}$ and *TBX5*$^{del/del}$ cells. **g, i,** UMAPs show clusters chosen for differential gene expression for comparison. **h, j,** Dot plots show top differentially expressed genes in each genetic background by *TBX5* genotype.

bioRxiv preprint doi: https://doi.org/10.1101/835603; this version posted November 10, 2019. The copyright holder for this preprint (which was not certified by peer review) is the author/funder, who has granted bioRxiv a license to display the preprint in perpetuity. It is made available under aCC-BY-ND 4.0 International license.

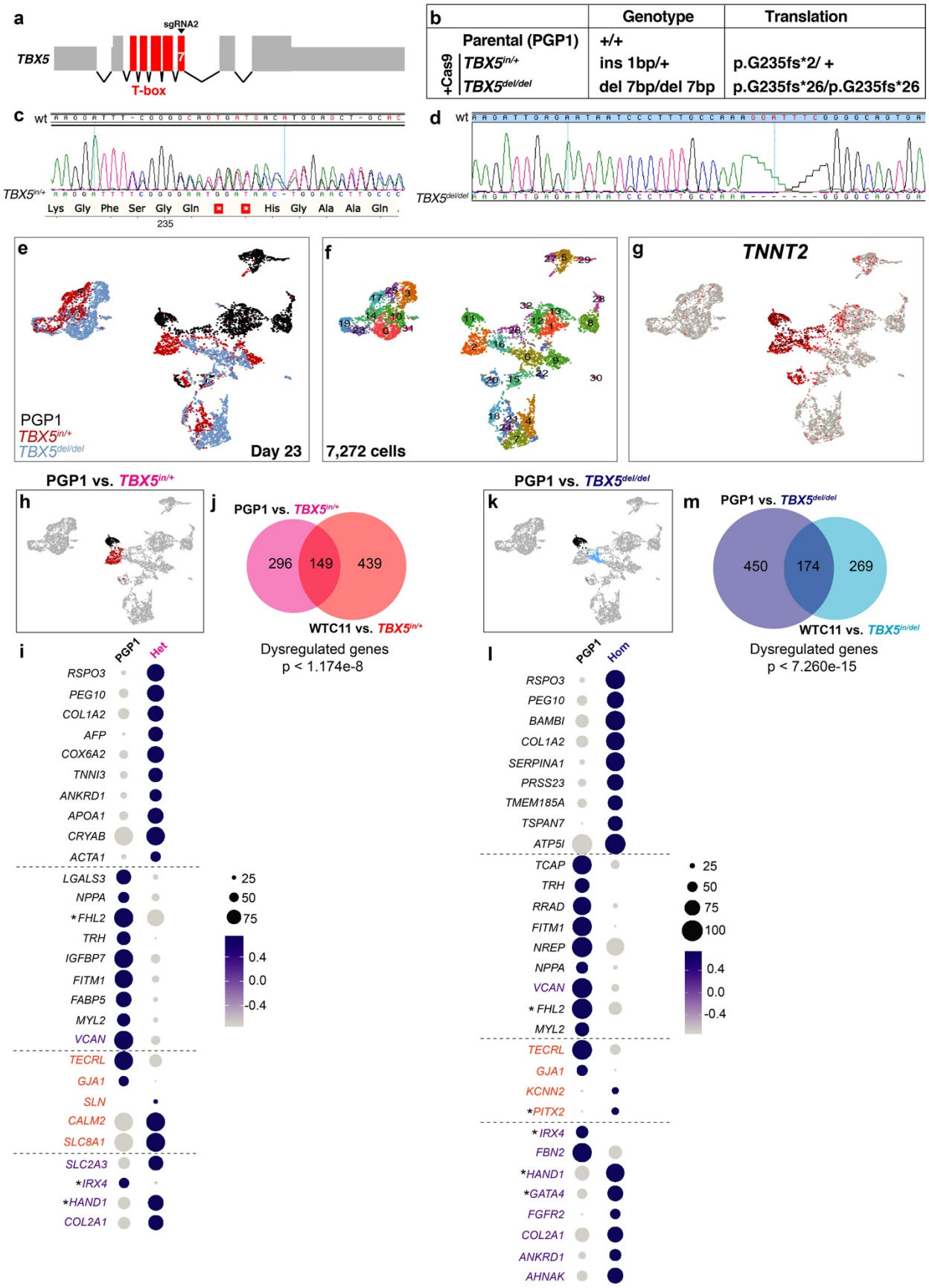

1136

bioRxiv preprint doi: https://doi.org/10.1101/835603; this version posted November 10, 2019. The copyright holder for this preprint (which was not certified by peer review) is the author/funder, who has granted bioRxiv a license to display the preprint in perpetuity. It is made available under aCC-BY-ND 4.0 International license.

Extended Data 11. Assessment of an alternative genetic background for TBX5 dose-sensitive gene expression. a, Diagram of human *TBX5* gene is shown, with exons in red. The guide sgRNA2 was used to target exon 7, which encodes a portion of the T-box domain, of *TBX5* in PGP1 iPS cells. **b,** Table specifies the nature of each *TBX5* mutation and the predicted translation of TBX5 for PGP1-derived $TBX5^{in/+}$ or $TBX5^{del/del}$ cells. **c, d,** Chromatogram indicates a 1 base pair insertion of the mutant *TBX5* allele for PGP1-derived $TBX5^{in/+}$ cells (**c**) or a 7 base pair deletion of *TBX5* in $TBX5^{del/del}$ cells (**d**). **e-g,** UMAPs of all cells from day 23 by *TBX5* genotype (**e**), cluster identity (**f**), or by *TNNT2* expression (**g**). **h, k,** UMAPs mark *TBX5* genotype-enriched clusters by color that were selected for differential gene expression test. **i, l,** Dot plots show top differentially expressed genes in (**i**) $TBX5^{in/+}$- or (**l**) $TBX5^{del/del}$-enriched clusters. Significance was determined by Wilcoxon Rank Sum test (adj p-value<0.05) (Supplementary Table 2). **j**, Venn diagram shows overlap of TBX5-dependent gene sets between differences of WTC11 and WTC11-derived $TBX5^{in/+}$ clusters and differences of PGP1 and PGP1-derived $TBX5^{in/+}$ clusters. **m,** Venn diagram displays overlap of TBX5-dependent gene sets between differences of WTC11 and WTC11-derived $TBX5^{in/del}$ and differences of PGP1 and PGP1-derived $TBX5^{del/del}$. Statistical significance was determined by Hypergeometric test, based on the union of highly variable genes from both datasets (2,566) as the population size.

bioRxiv preprint doi: https://doi.org/10.1101/835603; this version posted November 10, 2019. The copyright holder for this preprint (which was not certified by peer review) is the author/funder, who has granted bioRxiv a license to display the preprint in perpetuity. It is made available under aCC-BY-ND 4.0 International license.

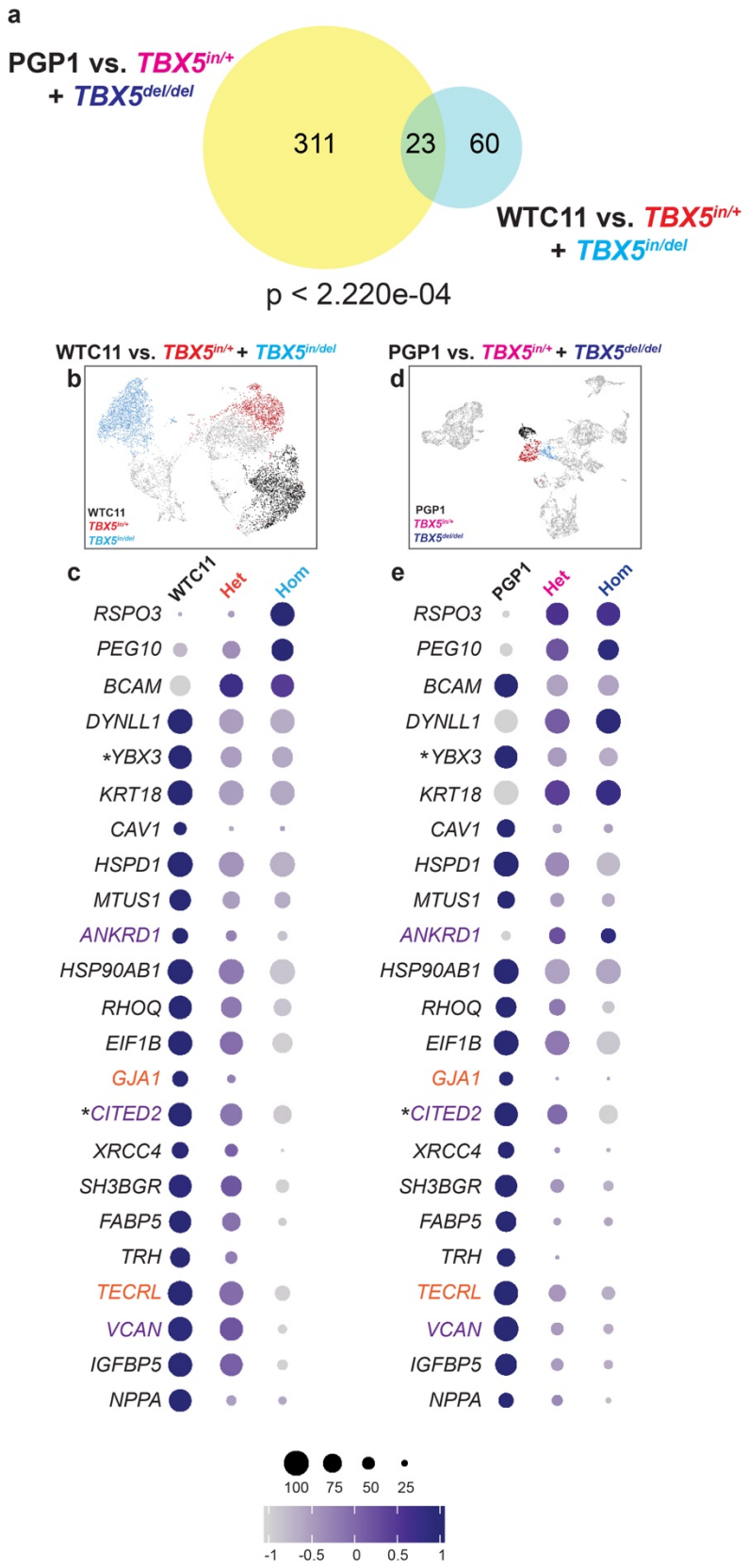

1158

bioRxiv preprint doi: https://doi.org/10.1101/835603; this version posted November 10, 2019. The copyright holder for this preprint (which was not certified by peer review) is the author/funder, who has granted bioRxiv a license to display the preprint in perpetuity. It is made available under aCC-BY-ND 4.0 International license.

Extended Data 12. Overlap of TBX5 dose-dependent genes between genetic backgrounds. a, Venn diagram shows overlap of differentially expressed genes between genetic backgrounds of WTC11-targeted *TBX5*$^{in/+}$ and *TBX5*$^{in/del}$ cells and PGP1-targeted *TBX5*$^{in/+}$ and *TBX5*$^{del/del}$ cells. Statistical significance was determined by Hypergeometric test, based on the union of highly variable genes from both datasets (2,566) as the population size. **b, d,** UMAPs show clusters chosen for differential gene expression for comparison. **c, e,** Dot plots show top differentially expressed genes in each genetic background by *TBX5* genotype (adj p-value<0.05 by Wilcoxon Rank Sum test).

bioRxiv preprint doi: https://doi.org/10.1101/835603; this version posted November 10, 2019. The copyright holder for this preprint (which was not certified by peer review) is the author/funder, who has granted bioRxiv a license to display the preprint in perpetuity. It is made available under aCC-BY-ND 4.0 International license.

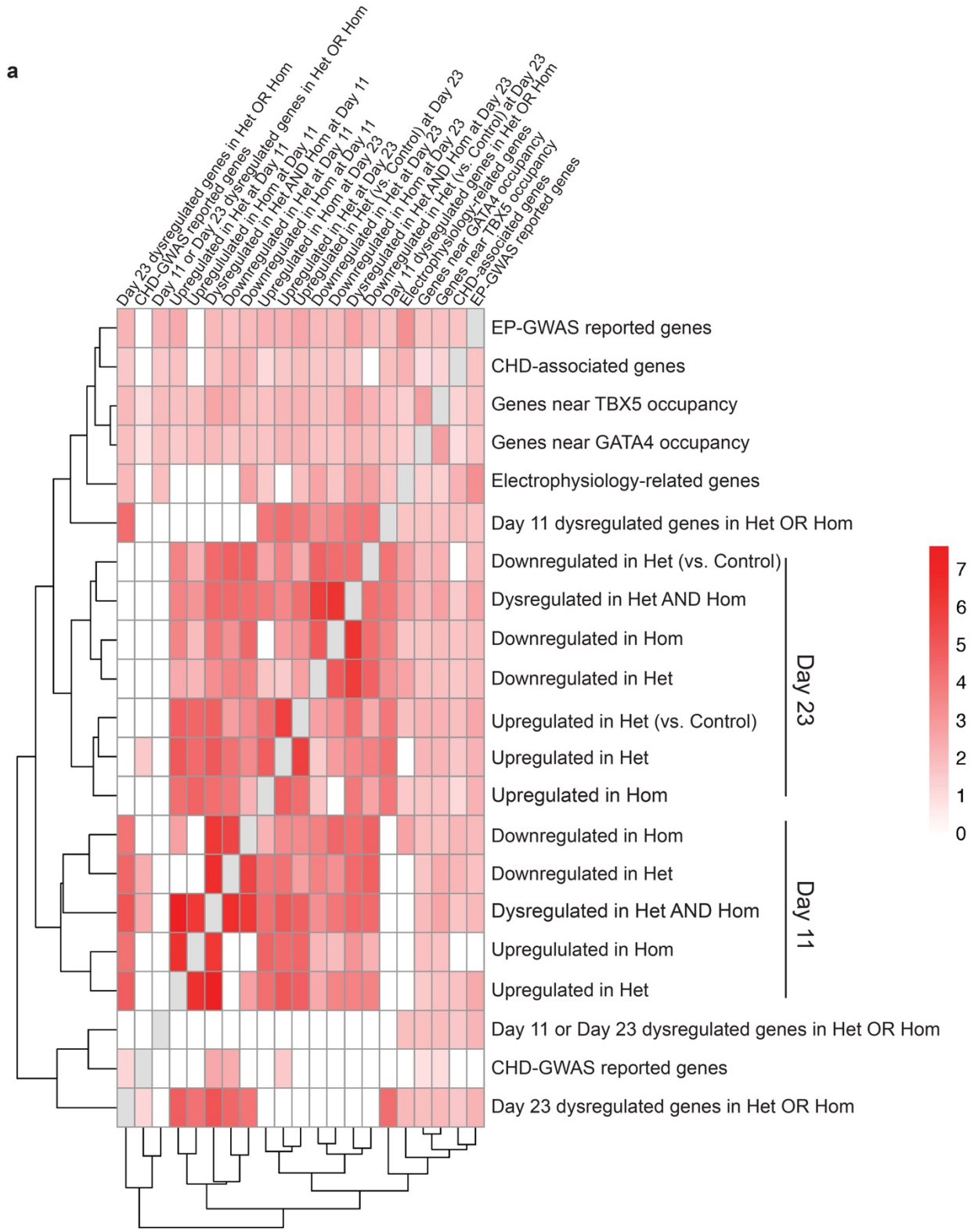

bioRxiv preprint doi: https://doi.org/10.1101/835603; this version posted November 10, 2019. The copyright holder for this preprint (which was not certified by peer review) is the author/funder, who has granted bioRxiv a license to display the preprint in perpetuity. It is made available under aCC-BY-ND 4.0 International license.

Extended Data 13. Associations between disease candidates, GWAS reported genes, TBX5 or GATA4 occupancy, or TBX5-dependent genes. a, Heat map indicates odds ratios (FDR<0.05) between several variables, including CHD-associated genes, EP-related genes, CHD-related GWAS reported genes, arrhythmia-related GWAS (EP-GWAS) reported genes, TBX5 or GATA4 occupancy, and TBX5-dependent gene sets at day 11 or day 23 (Supplementary Table 4). Statistical significance was determined by Benjamini-Hochberg multiple testing.

bioRxiv preprint doi: https://doi.org/10.1101/835603; this version posted November 10, 2019. The copyright holder for this preprint (which was not certified by peer review) is the author/funder, who has granted bioRxiv a license to display the preprint in perpetuity. It is made available under aCC-BY-ND 4.0 International license.

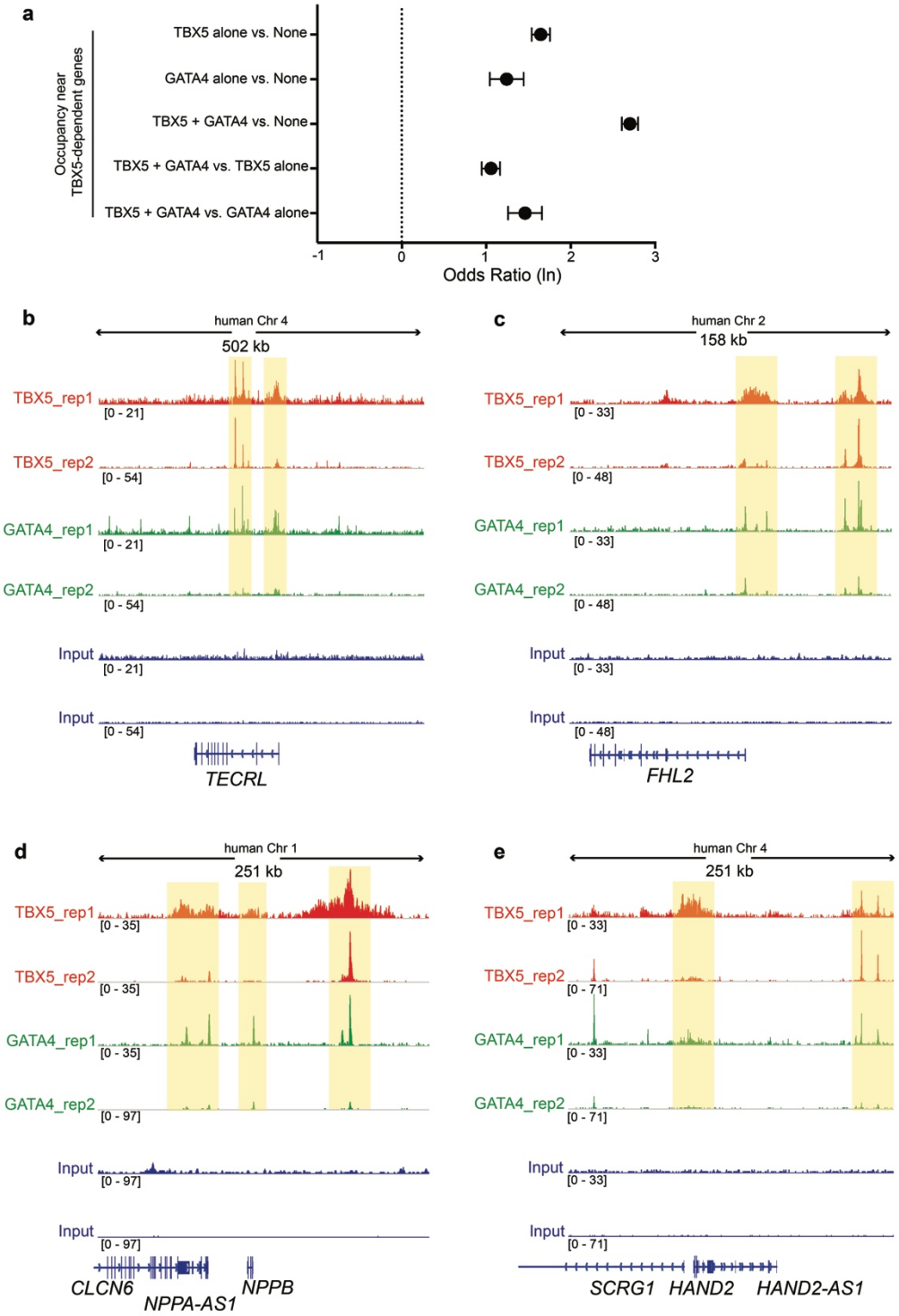

1182

bioRxiv preprint doi: https://doi.org/10.1101/835603; this version posted November 10, 2019. The copyright holder for this preprint (which was not certified by peer review) is the author/funder, who has granted bioRxiv a license to display the preprint in perpetuity. It is made available under aCC-BY-ND 4.0 International license.

Extended Data 14. Co-occupancy of TBX5 or GATA4 near human TBX5-dependent genes.
a, Odds ratios (FDR<0.05) of TBX5, GATA4 or TBX5 and GATA4 occupancy near all human TBX5-dependent genes. Statistical significance was determined by Benjamini-Hochberg multiple testing (Supplementary Table 5). **b,** Browser tracks of TBX5 and GATA4 occupancy from iPS cell-derived cardiomyocytes are shown for loci of TBX5-dependent genes *TECRL, FHL2, NPPA/NPPB* or *HAND2.*

bioRxiv preprint doi: https://doi.org/10.1101/835603; this version posted November 10, 2019. The copyright holder for this preprint (which was not certified by peer review) is the author/funder, who has granted bioRxiv a license to display the preprint in perpetuity. It is made available under aCC-BY-ND 4.0 International license.

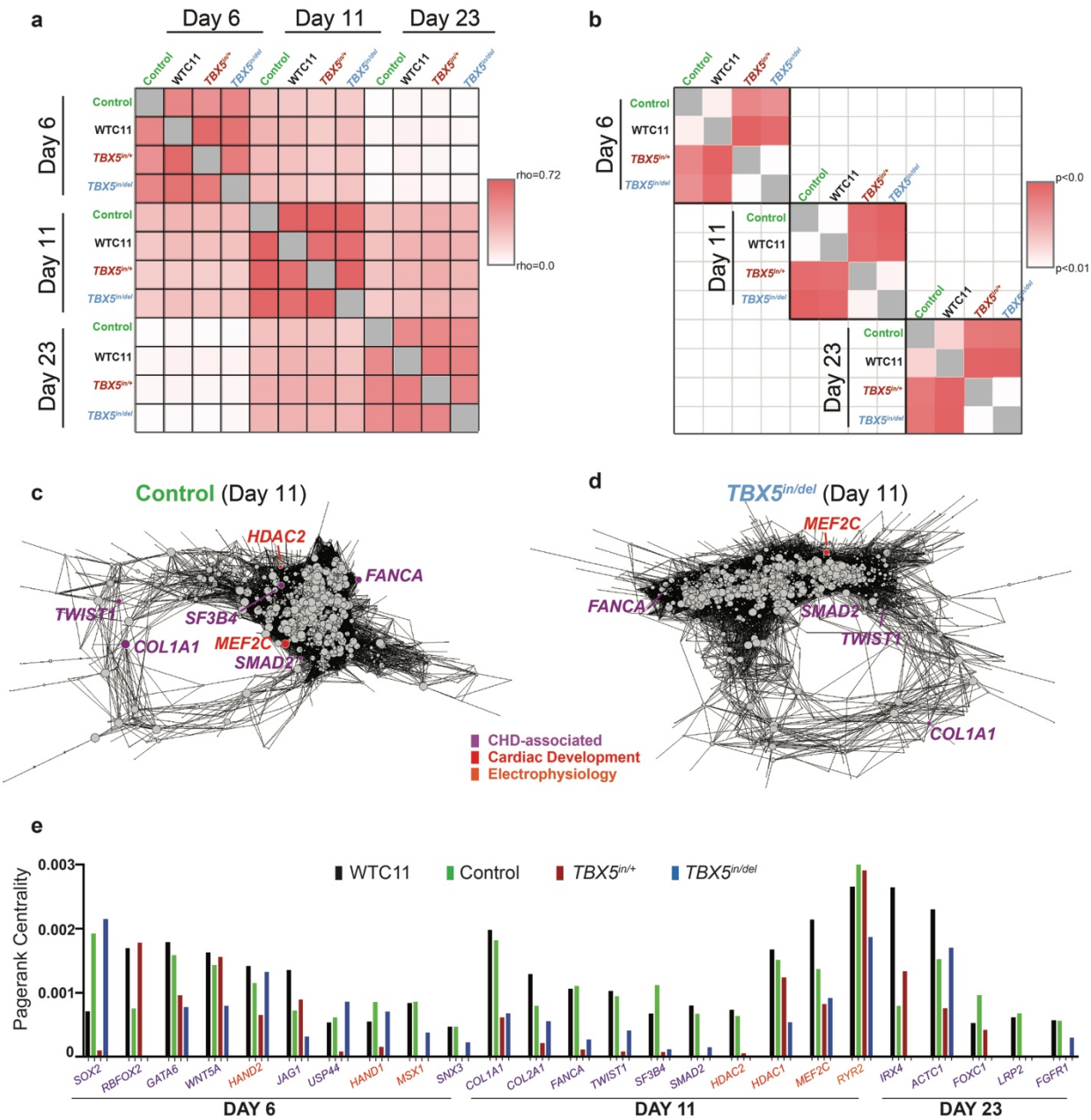

Extended Data 15. Analysis of TBX5 dosage-sensitive gene regulatory networks. **a,** Correlation plot (Pearson correlations of pagerank centralities) of networks by genotypes and time points are shown. Note that networks display highest similarity (red) within a time point. An inter-stage dissimilarity (white) grows proportionally to the time difference (i.e. Day 23 is less similar to Day 6 than Day 11). Therefore, comparisons for genotype differences were made within differentiation stages. **b,** Network similarity among genotypes within each time point is shown (Wilcoxon Rank Sum test of pagerank centralities for nodes from selected time point comparisons). **c, d,** Network diagrams of day 11 cardiomyocytes for control (**c**) or *TBX5*$^{in/del}$ (**d**) are shown. **e**, Quantification of pagerank centrality for significantly altered (top 5% cutoff) nodes of CHD-associated or heart development genes at specific time points are shown.

bioRxiv preprint doi: https://doi.org/10.1101/835603; this version posted November 10, 2019. The copyright holder for this preprint (which was not certified by peer review) is the author/funder, who has granted bioRxiv a license to display the preprint in perpetuity. It is made available under aCC-BY-ND 4.0 International license.

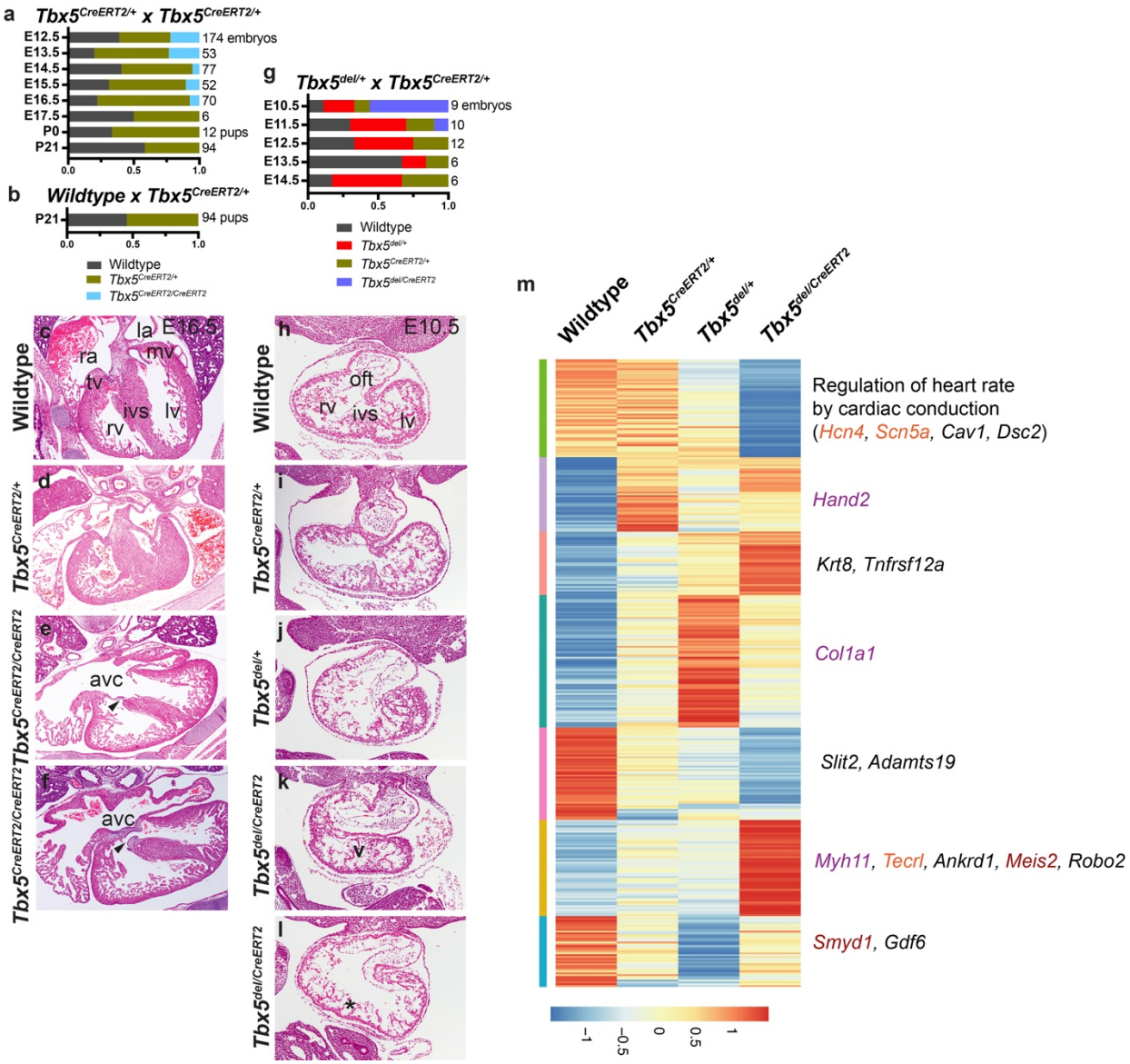

Extended Data 16. An allelic series of *Tbx5* mutants in mouse. a, Embryos or pups from matings of *Tbx5*$^{CreERT2/+}$ X *Tbx5*$^{CreERT2/+}$ were genotyped. Expected Mendelian ratios were not observed for *Tbx5*$^{CreERT2/CreERT2}$ after E13.5. **b,** Expected Mendelian ratios were observed for pups at weaning from matings of *Tbx5*$^{CreERT2/+}$ X wildtype. **c-f,** Transverse sections of hearts at embryonic day 16.5 (E16.5) from each genotype are shown. Right atrium (ra), left atrium (la), right ventricle (rv), left ventricle (lv), tricuspid valve (tv), mitral valve (mv) and interventricular septum (ivs) are labeled. Note atrioventricular canal defects (avc), which includes membranous VSDs (arrowheads), in *Tbx5*$^{CreERT2/CreERT2}$ hearts (**e, f**). **g,** Expected Mendelian ratios from matings of *Tbx5*$^{CreERT2/+}$ X *Tbx5*$^{del/+}$ were not observed for *Tbx5*$^{del/CreERT2}$ after E10.5. **h-l,** Transverse sections of individual hearts at embryonic E10.5 from each genotype are shown. Note a single ventricle (v) and lack of invagination (*) at the site of the nascent interventricular groove. **m,** Heat map by genotype of average gene expression data from 4 individual whole hearts at E10.5 (Supplementary Table 7). Significant GO term (adj p-value <0.05) for one cluster is shown, including underlying genes. TBX5-dependent mouse genes that are also

bioRxiv preprint doi: https://doi.org/10.1101/835603; this version posted November 10, 2019. The copyright holder for this preprint (which was not certified by peer review) is the author/funder, who has granted bioRxiv a license to display the preprint in perpetuity. It is made available under aCC-BY-ND 4.0 International license.

TBX5-sensitive in human cells are shown. CHD-associated (purple), electrophysiology-related (orange), or heart development (red) genes are highlighted.

bioRxiv preprint doi: https://doi.org/10.1101/835603; this version posted November 10, 2019. The copyright holder for this preprint (which was not certified by peer review) is the author/funder, who has granted bioRxiv a license to display the preprint in perpetuity. It is made available under aCC-BY-ND 4.0 International license.

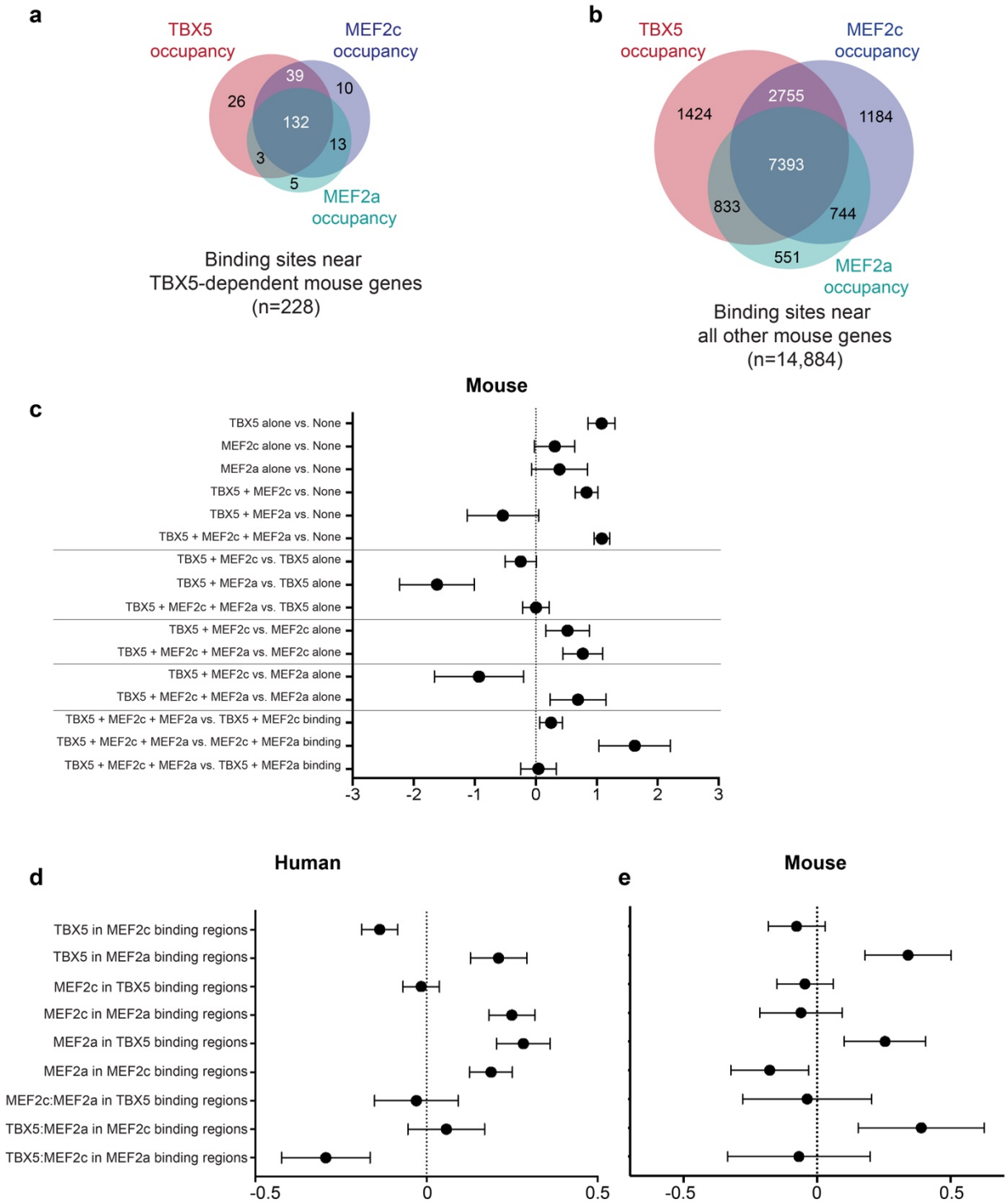

Extended Figure 17. Analyses of TBX5, MEF2c and MEF2a co-occupancy. a, b, Venn diagrams display the overlap of TBX5, MEF2a or MEF2c occupancy near mouse orthologs of human TBX5-dependent or -independent genes, respectively. **c,** Odds ratios (FDR<0.05) of combinations of TBX5, MEF2a or MEF2c occupancy near TBX5-dependent mouse genes

bioRxiv preprint doi: https://doi.org/10.1101/835603; this version posted November 10, 2019. The copyright holder for this preprint (which was not certified by peer review) is the author/funder, who has granted bioRxiv a license to display the preprint in perpetuity. It is made available under aCC-BY-ND 4.0 International license.

(Supplementary Table 5). **d, e,** Odds ratios (FDR<0.05) of combinations of MEF2a or MEF2c occupancy within 1kb of TBX5 binding sites near TBX5-dependent or all other genes in human (**d)** or mouse (**e**) (Supplementary Table 8).

bioRxiv preprint doi: https://doi.org/10.1101/835603; this version posted November 10, 2019. The copyright holder for this preprint (which was not certified by peer review) is the author/funder, who has granted bioRxiv a license to display the preprint in perpetuity. It is made available under aCC-BY-ND 4.0 International license.

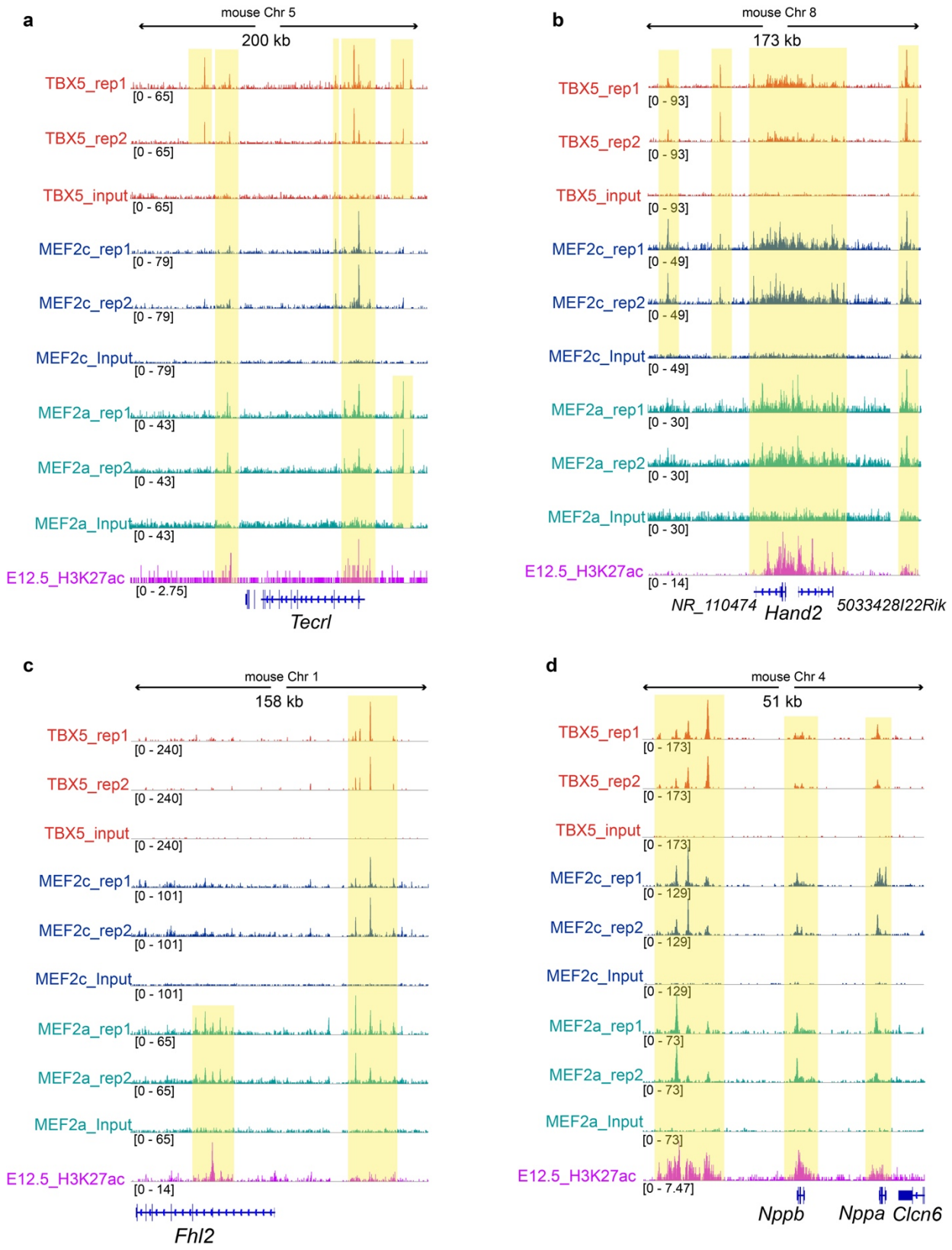

1238

bioRxiv preprint doi: https://doi.org/10.1101/835603; this version posted November 10, 2019. The copyright holder for this preprint (which was not certified by peer review) is the author/funder, who has granted bioRxiv a license to display the preprint in perpetuity. It is made available under aCC-BY-ND 4.0 International license.

Extended Data 18. Co-occupancy of TBX5, MEF2a and MEF2c near TBX5-dependent genes. a-d, Browser tracks for ChIP-seq data from E12.5 hearts of TBX5, MEF2c, MEF2a and H3K27ac near conserved TBX5-dependent genes, *Hand2*, *Tecrl, Fhl2* and *Nppa/Nppb*. Yellow bands of shading indicate co-occupancy that is present in replicates but not in input.

bioRxiv preprint doi: https://doi.org/10.1101/835603; this version posted November 10, 2019. The copyright holder for this preprint (which was not certified by peer review) is the author/funder, who has granted bioRxiv a license to display the preprint in perpetuity. It is made available under aCC-BY-ND 4.0 International license.

Extended Data 19. Correlations of between disease candidates, GWAS reported genes, TBX5, MEF2c or MEF2a occupancy, or TBX5-dependent genes. a, Heat map indicates odds ratios (FDR<0.05) between several variables, including CHD-associated genes, EP-related genes, CHD-related GWAS reported genes, arrhythmia-related GWAS (EP-GWAS) reported genes, TBX5, MEF2c, or MEF2a occupancy, and TBX5-dependent human gene sets at day 11

bioRxiv preprint doi: https://doi.org/10.1101/835603; this version posted November 10, 2019. The copyright holder for this preprint (which was not certified by peer review) is the author/funder, who has granted bioRxiv a license to display the preprint in perpetuity. It is made available under aCC-BY-ND 4.0 International license.

or day 23 or TBX5-dependent mouse gene sets (Supplementary Table 6). Statistical significance was determined by Benjamini-Hochberg multiple testing.

bioRxiv preprint doi: https://doi.org/10.1101/835603; this version posted November 10, 2019. The copyright holder for this preprint (which was not certified by peer review) is the author/funder, who has granted bioRxiv a license to display the preprint in perpetuity. It is made available under aCC-BY-ND 4.0 International license.

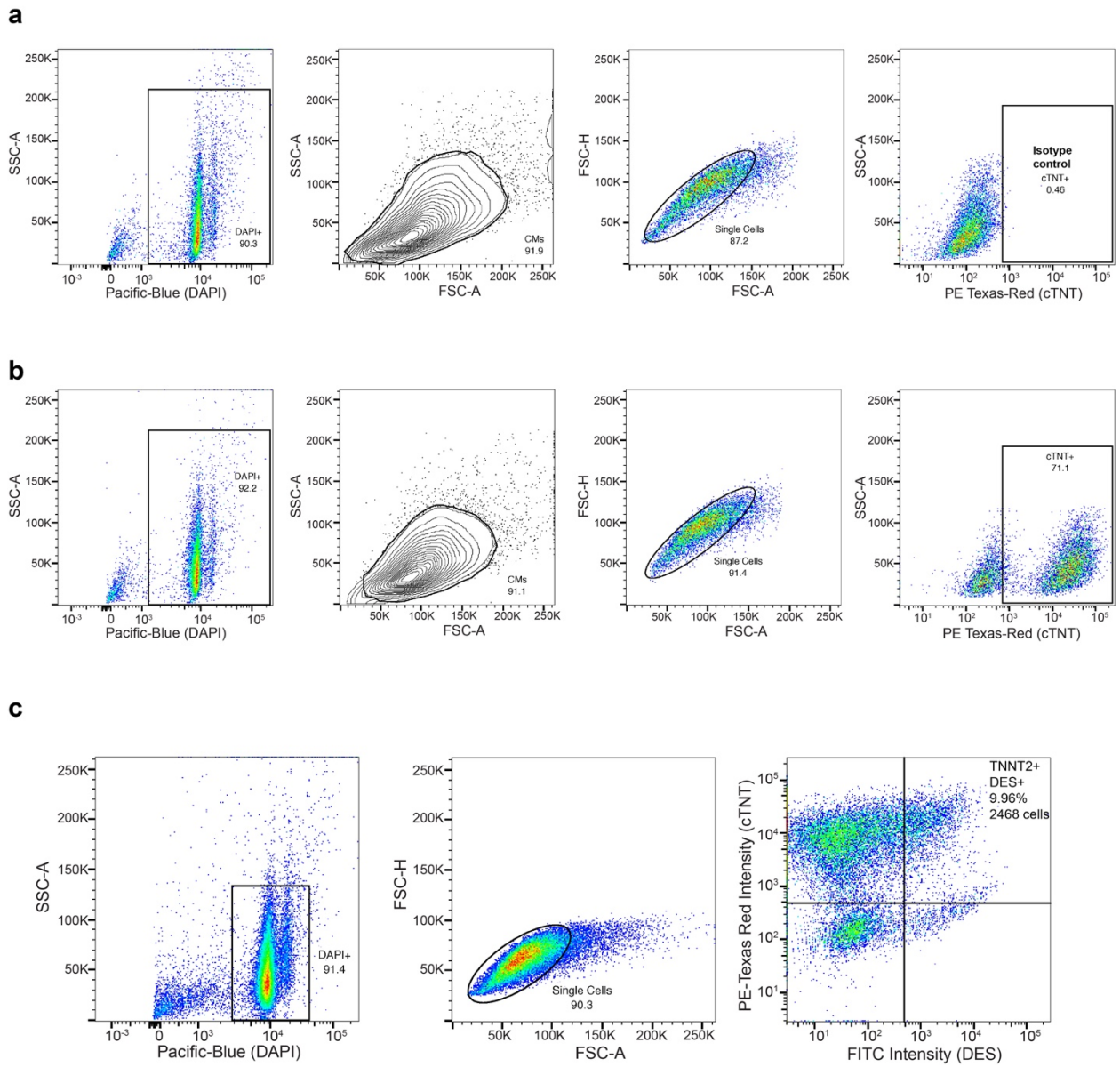

Extended Data 20. Gating strategies for flow cytometry. a, b, Gates were determined in each of the isotype controls per genotype and applied to genotype-matched samples. First, gates were drawn around DAPI$^+$ cells in SSC-A vs. Pacific-Blue plots. Next, SSC-A vs. FSC-A plots were used to exclude debris. Single cells were then isolated by gating of FSC-H vs. FSC-A plots. cTNT$^+$ gates were drawn in SSC-A vs. FITC plots. **c,** For cTNT$^+$/DES$^+$ cells, PE-Texas Red vs. FITC plots were used.

bioRxiv preprint doi: https://doi.org/10.1101/835603; this version posted November 10, 2019. The copyright holder for this preprint (which was not certified by peer review) is the author/funder, who has granted bioRxiv a license to display the preprint in perpetuity. It is made available under aCC-BY-ND 4.0 International license.

Supplementary Tables.

Supplementary Table 1. Curated gene lists, which are used in this study, include electrophysiology (EP)-related genes, human congenital heart disease (CHD)-associated genes, mouse CHD-associated genes and cardiac development-related genes.

Supplementary Table 2. Lists of differential genes from comparisons between *TNNT2*$^{+}$ clusters, at day 11 or day 23, or by biological replicate or genetic background at day 23.

Supplementary Table 3. TBX5-sensitive gene regulatory network analyses, by pagerank or degree, or by correlation with *TBX5* or *MEF2C* expression.

Supplementary Table 4. Data for odds ratios for correlation of human TBX5-dependent genes near TBX5 or GATA4 occupancy, congenital heart disease (CHD)-associated GWAS, electrophysiology (EP)-related GWAS, CHD-associated genes, or EP-related genes.

Supplementary Table 5. Odds ratios for co-occupancy data near human TBX5-dependent genes for TBX5 and GATA4, or for co-occupancy of TBX5, MEF2c and MEF2a near human or mouse TBX5-dependent genes.

Supplementary Table 6. Data for odds ratios for correlation of human or mouse TBX5-dependent genes near TBX5, MEF2c or MEF2a occupancy, congenital heart disease (CHD)-associated GWAS, electrophysiology (EP)-related GWAS, CHD-associated genes, or EP-related genes.

Supplementary Table 7. Bulk RNAseq data of mouse embryonic hearts at E10.5 for an allelic series of *TBX5* mutants.

Supplementary Table 8. Odds ratio for transcription factor (TF) binding of TBX5, MEF2c, or MEF2a within 1kb of the other TFs in the trio, near human or mouse TBX5-depenedent genes.